VOID HUNTING: AMBIENT NOISE TOMOGRAPHY FOR SPATIO-TEMPORAL SUBSURFACE IMAGING AND MONITORING IN KARST ENVIRONMENTS

by
John B. Paustian

A thesis

submitted in partial fulfillment

of the requirements for the degree of

Master of Science in Geophysics

Boise State University

August 2021

BOISE STATE UNIVERSITY GRADUATE COLLEGE

DEFENSE COMMITTEE AND FINAL READING APPROVALS

of the thesis submitted by

John B. Paustian

Thesis Title: Void Hunting: Ambient Noise Tomography for Spatio-Temporal Subsurface Imaging and Monitoring in Karst Environments

Date of Final Oral Examination: 1 April 2021

The following individuals read and discussed the thesis submitted by student John B. Paustian, and they evaluated the student's presentation and response to questions during the final oral examination. They found that the student passed the final oral examination.

Dylan Mikesell Ph.D.	Chair, Supervisory Committee
Lee Liberty M.S.	Member, Supervisory Committee
Qifei Niu Ph.D.	Member, Supervisory Committee

The final reading approval of the thesis was granted by Dylan Mikesell Ph.D., Chair of the Supervisory Committee. The thesis was approved by the Graduate College.

DEDICATION

To my parents, for helping to cultivate a growth mindset and reminding me to keep my head when those around me are losing theirs.

ACKNOWLEDGMENT

I would first like to thank my committee members for their guidance and flexibility: Dylan Mikesell, Lee Liberty and Qifei Niu.

An integral part of this thesis are the scientists who collected the data in Florida that made the research possible: Dylan, Zongbo Xu and Thomas Otheim from Boise State University, Niels Grobbe and Stéphanie Barde-Cabusson from the University of Hawaii at Manoa and Sarah Kruse and Tonian Robinson from the University of South Florida. Additionally, I would like to acknowledge Thomas Lecocq and Aurélien Mordret for their assistance with the MSNoise software package.

Thank you to everyone not already mentioned from Boise State who took an interest in my continued development as a geoscientist, including Shawn Benner, Jim McNamara, Jake "The Condor" Anderson, Nick Pollock, Gabe Gribler, Alex Witsil and Diego Domenzain.

This thesis would not be complete without mentioning Colby Meyer and Jaron Hathaway for saving my life during the summer rattlesnake discovery tour...I don't want to, but I will!

Finally, thank you to Leah for always having my back.

ABSTRACT

Karst environments are characterized by voids, i.e. sinkholes and conduits of varying size that arise from the active dissolution of carbonate rock by acidic groundwater. These voids, whether air-, water-, or soil-filled, can be difficult to image using near-surface geophysical methods due to the limited investigation depths of most active-source methods. In addition, due to the significant effort it takes to collect active-source data, investigators are often unable to monitor spatio-temporal variations in the subsurface. The ability to detect, image, and monitor subsurface voids improves the understanding of processes that create and transform voids, a vitally important insight across a variety of scientific disciplines and engineering applications, including hydrogeology, geotechnical engineering, planetary science and even issues of national security. Using a 54-element nodal array (1C and 3C sensors), I image the subsurface of the USF GeoPark with ambient noise surface wave tomography. I also use complementary active-source geophysical datasets (e.g. 2D ERT) collected at the GeoPark to constrain and/or validate the tomography results. I address two research questions with this study: (1) How do ambient seismic methods complement active-source near-surface methods? (2) Can ambient noise tomography resolve voids in the karst environment? In this thesis, I discuss my answers to these questions and present the current state of surface wave methods in the karst environment, including the feasibility for utilizing ambient noise methods to monitor spatio-temporal changes

in sinkhole and conduit formation. In addition to the ability to use seismic methods for temporal monitoring, ambient noise provides lower frequencies than what are achievable with active-source seismic methods. Using frequencies from 5-28 Hz, ambient noise tomography is able to image deeper into the subsurface (up to 100 m at 5 Hz) than previous active-source seismic studies at the GeoPark field site. This study yields a more robust and simple method to image voids in covered karst environments and a long-term installation of ambient seismic nodes enables future investigations of spatio-temporal variations in void structures.

TABLE OF CONTENTS

LIST OF FIGURES

LIST OF TABLES

CHAPTER 1:

INTRODUCTION

1.1 Significance & Scientific Problem

Combined with a greater understanding of groundwater fluxes in a karst aquifer for modeling drinking water reservoirs, temporal structure resolution allows for advanced hazard forecasting and mitigation in developed areas prone to sinkhole formation. Florida has arguably the most economic development over karst environments in the world, making the characterization of sinkhole development vitally important for both water management and public safety (Park & Taylor, 2010; Bumpus & Kruse, 2014).

This research focuses on the west-central coast of Florida, specifically the GeoPark site on the campus of the University of South Florida in Tampa. Intended as a geologic education site, the GeoPark is undeveloped and is an excellent example of a covered karst landscape, where the weathered limestone aquifer is covered by a layer of fine sand, rendering the surface topography extremely flat.

Karst environments are dynamic geologic environments characterized by voids or cavities that are developed from the dissolution and erosion of high-solubility carbonate rock by acidic groundwater flow (Miller, 1990). Characteristic features of karst environments include sinkholes, springs, caves and extensive connected subsurface drainage networks, or conduits, all of which involve void structures (Parker, 1992;

Tihansky, 1999).

A void in this context refers to an opening within the carbonate host rock that can be filled with air, water, or sediment. In a covered karst system, voids are typically filled by sediment, called conduit fill. A conduit is a roughly vertical void space left in the carbonate host rock by the dissolution of acidic groundwater. Conduits in karst environments frequently collapse over time, forming what is commonly referred to as a sinkhole. Sinkholes in covered karst environments are typically filled and covered by a mantle of typically insoluble sand, silt and clay deposits (Tihansky, 1999; Bumpus & Kruse, 2014). The surface expression of a sinkhole can vary depending on the level of sediment cover and the time elapsed since the collapse of the underlying conduit. However, the subsurface expression of the sinkhole or collapsed conduit will generally maintain the original relationship of a void structure within the host rock that contains conduit fill, and will therefore be detectable using geophysical methods.

The temporal natural of dynamic karst environments manifests though two primary time scale drivers: The short-term response of a karst aquifer over hours or days depends greatly on the long-term evolution of the landscape through the development of fractures, increased porosity and voids, which can occur over tens of thousands of years (Kaufmann, 2009). Groundwater flow through a drainage network within a karst aquifer experiences variation on the scale of minutes, hours or days. Conduit collapse can occur abruptly and without warning, but the development of void structures in karst is a much longer process.

Difficulty in imaging voids and cavities in the subsurface, along with an absence of temporal resolution, leads to additional geoscientific and engineering problems. From a hydrological perspective, voids permit percolation and develop zones of preferential

aquifer recharge (Parker, 1992; Kruse *et al.*, 2006). Visualizing and quantifying the dynamic structure of these systems over time is crucial for understanding groundwater flux and storage in carbonate aquifers, particularly for drinking water (Bumpus & Kruse, 2014). Understanding the structure of karst environments is crucial for groundwater studies in carbonate rock as sinkholes and associated conduits serve as zones of preferential recharge to the underlying aquifer (Kruse *et al.*, 2006; Bumpus & Kruse, 2014). Changes in karst environments may also constitute a public health issue. As illustrated in Figure 1.1, carbonate aquifers make up 20% of the land area of the United States (Maupin & Barber, 2000) and are relied on for drinking water by 25% of the world's population (White *et al.*, 2016).

Voids also present an issue for geotechnical engineers. Early risk assessment and monitoring of sinkholes and related ground subsidence is of paramount importance for infrastructure and economic development in urban areas and can minimize financial and societal disruption (Park & Taylor, 2010). Ground subsidence from sinkholes is a hazard affecting site stability and building and road integrity in regions where karst is the predominant geomorphic process (Tihansky, 1999; Kruse *et al.*, 2006).

Outside of terrestrial karst environments, subsurface voids are of recent interest to planetary scientists. Voids in planetary pseudokarst environments, i.e. voids or caves formed in volcanic rock that resemble carbonate karst structures, are thought to be a likely storage site for water ice (Williams *et al.*, 2010) and may very well conceal signs of life on other planets (Boston *et al.*, 1992, 2001; Boston, 2010).

As with naturally-forming sinkholes and conduits in carbonate rock, detection methods can also be applied to anthropogenic voids. Locating voids in the form of clandestine tunnels is a national security concern both overseas and along our

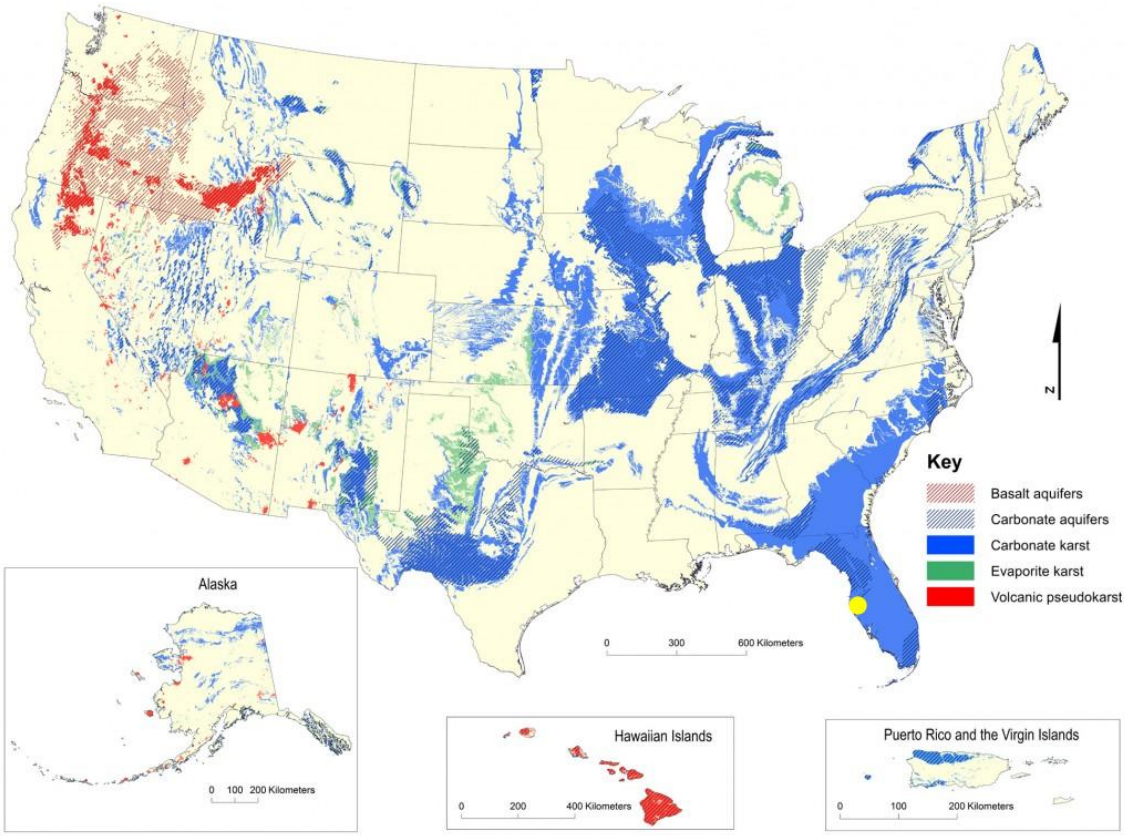

Figure 1.1 Map of karst and pseudokarst aquifers in the United States. The GeoPark study area in Tampa, Florida is denoted in yellow.

domestic borders. There is an urgent need to develop techniques for the detection and monitoring of such tunnels used for illicit activities as in Sloan *et al.* (2015).

Geophysical methods are a useful tool for investigating and identifying features of karst environments. These methods are particularly useful when working from a conceptual model of an area with a suspected subsurface structure of interest.

However, subsurface voids and cavities in karst environments are notoriously difficult to image (Park & Taylor, 2010; Sloan *et al.*, 2015). While commonly used as a means of sinkhole detection, high-frequency GPR and DC resistivity geophysical methods are often unable to probe deep enough to clearly image such structure present in karst environments; they are often limited to a frequency-dependent exploration depth of about 10 m. As karst environments are dynamic, geophysical monitoring is vital, yet underutilized. Though shallow geophysical methods for sinkhole detection are well-established (e.g., Dobecki & Upchurch, 2006; Kruse *et al.*, 2006; Park & Taylor, 2010; Bumpus & Kruse, 2014), current active-source methods neglect spatio-temporal variation in the subsurface.

There are two primary science problems addressed by my research. (1) Subsurface voids and cavities are difficult to image with geophysical methods and (2) it is even more difficult and expensive to monitor spatio-temporal changes of voids in dynamic environments.

1.2 Rock Physics

Seismology gives information about the mechanical properties of materials in the subsurface. Based on the rough stratigraphy from previous studies at the GeoPark site (e.g., Parker, 1992; Kruse *et al.*, 2006; Park & Taylor, 2010), I expect large contrasts in mechanical properties between the limestone of the bedrock and the

Table 1.1 NEHRP site classifications for seismic provisions for new build-ing construction.

Site Class	Shear Wave Velocity (Vs) (m/s)
A (Hard Rock)	>1500
B (Rock)	760-1500
C (Very dense soil and soft rock)	360-760
D (Stiff soil)	180-360
E (Soft clay soil)	<180
F (Soils requiring additional response)	<180 and meeting additional conditions

sediment both filling voids and within the shallow overburden. If the voids were filled with air or water, the shear wave velocity would effectively be zero due to the inability of fluids to support shear stresses.

Table 1.1 shows the NEHRP (National Earthquake Hazards Reduction Program) site classification shear wave velocity criteria (Building Seismic Safety Council (BSSC), 2003). While not strictly pertinent to this particular site as no future development is planned, site classification allows for a velocity comparison between varying types of soil and rock while also placing constraints on geotechnical site preparation for future construction. At this site, I expect shear wave velocities corresponding to site classes A, B, C, and D, hard rock to stiff soil. I also expect a large shear wave velocity contrast between class A (hard rock: unweathered limestone bedrock) and class D (stiff soil: sand, silt clay conduit fill). Using ambient noise tomography, I will resolve the difference between the two soil site classes in order to isolate and characterize soil-filled voids within the limestone.

Table 1.2 Geophysical methods, measured parameters and physical prop-erties.

Geophysical Method	Physical Property
Self potential (SP)	Natural electrical potentials
DC resistivity	Electrical resistivity
GPR	Dielectric constant, magnetic permeability, conductivity
Seismic	Acoustic velocity (function of elastic moduli and density)

The geophysical methods employed in this study are sensitive to a variety of physical properties, specifically the contrasts of these properties between different geological materials. These properties are described in Table 1.2 (Kruse *et al.*, 2006; Anderson *et al.*, 2008).

Sinkholes and other void structures in a covered karst environment have the following geophysical signatures: For the self potential method, a strong negative electrical potential anomaly is indicative of preferential gravity-driven flow, such as through a vertical conduit (Grobbe & Barde-Cabusson, 2019). Similarly, a heterogeneous resistivity distribution showing lateral variation with zones of increased conductivity indicate increased saturation within the host bedrock, another feature of conduit-type structure in karst (Kruse *et al.*, 2006; Kaufmann, 2014). Depressions occurring in brightly reflective radar horizons in covered karst environments are likely clay-rich layers settling in the top of a sinkhole (Kruse *et al.*, 2006). Finally, shear wave velocity heterogeneities found using a seismic survey, in particular low velocity anomalies within a higher velocity host rock, can be diagnostic for sediment-filled voids within consolidated bedrock (Park & Taylor, 2010).

1.3 Knowledge Gap

Large-scale sinkhole detection using geophysical methods is well-established; however, information about the temporal variation and development or formation of sinkholes and conduits is not available through active-source geophysical surveys without significant cost. Efforts have been made to image voids in the subsurface using active seismic techniques, but ambient noise tomography is still untested and potentially underutilized for the detection and monitoring of subsurface voids. Ambient seismic surveys enable long-term and periodic analysis of groundwater-flow and hazard sites for development in karst environments. A knowledge gap exists in regard to spatio-temporal imaging of voids such as sinkholes and conduits using ambient noise tomography and monitoring methods. We do not know which karst features can be imaged using ambient noise tomography, or the resolution with which those features can be imaged.

1.4 Science Questions

There are two questions to be answered by this research: (1) Can ambient noise tomography resolve voids in the karst environment? (2) How do ambient seismic methods complement active-source near-surface geophysical methods?

In Chapter 8, I will also discuss the implication of employing ambient noise methods to monitor spatio-temporal changes in the subsurface and present my observations and recommendations for additional research on the subject.

1.5 Activities & Implications of Research

In this thesis I apply established principles of seismic interferometry to study the passive imaging problem in a karst environment using surface wave ambient noise

tomography. I compare ambient noise tomography images to tomography resolved using a suite of commonly-used active-source geophysical methods. My objective is to improve the vertical and horizontal resolution of shear wave velocity structures in covered karst conduit systems for further research into void detection including aquifer resource characterization and groundwater drawdown and recharge studies in karst and pseudokarst environments. I also assess the feasibility of ambient noise tomography for sinkhole detection and conduit imaging.

Additionally, this research will develop novel techniques for imaging voids in the subsurface that can be applied to planetary science and national security interests such as the detection of clandestine tunnels (e.g., Sloan *et al.*, 2015).

1.6 Background

1.6.1 Study Area

The data used in this study come from the GeoPark, located on the campus of the University of South Florida (USF), shown in Figure 1.2. The GeoPark is a 22 acre area of undeveloped covered karst landscape designated for geological research and demonstrations (Kruse *et al.*, 2006). The GeoPark research site has been the focus of a host of geophysical studies relating to the structure and integrated hydrogeology of covered karst systems. Parker (1992) carried out an analysis of the stratigraphy and hydraulic properties of this area that have been used to corroborate results from many of the studies discussed in Section 1.6.2.

As with most of Florida, the USF GeoPark sits over the Floridian limestone and dolostone aquifer. The study site is marked in yellow in Figure 1.1, and sits on the western Gulf coast of Florida (Tihansky, 1999). West-Central Florida has a

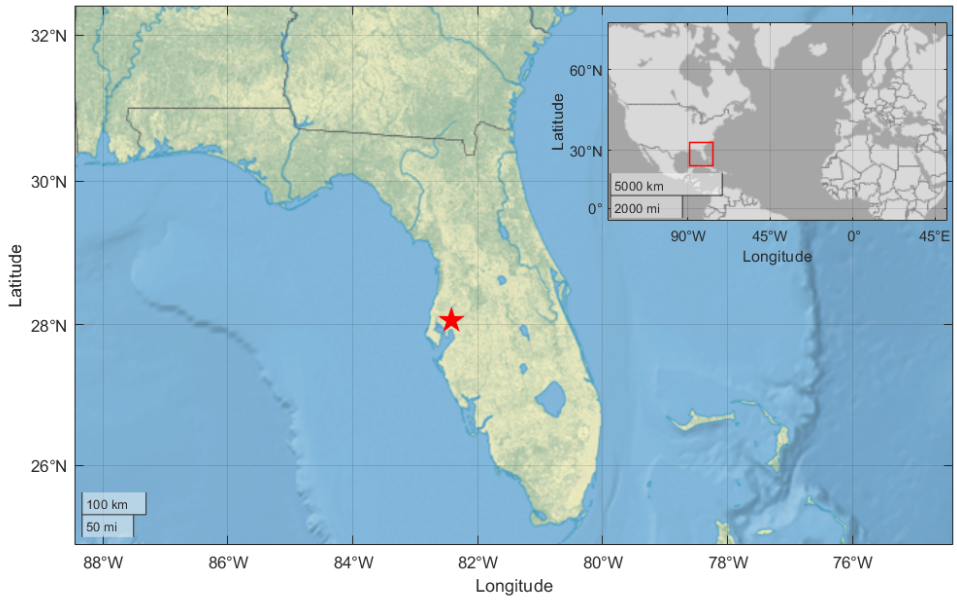

Figure 1.2 Location of the USF GeoPark in Tampa, Florida, USA.

shallow sand-silt-clay mantle no more than 10 m thick (Park & Taylor, 2010). The lithology at the GeoPark site is characterized by 3 to 5 m of loose aeolian sands and silt forming a surficial water table aquifer above a 3 m confining layer of sandy clay (Parker, 1992). Clay content increases with depth, and sandy clay abuts the heavily weathered limestone of the carbonate aquifer at depths of approximately 7-8 m (Bumpus & Kruse, 2014). While the surface of the limestone layer is highly irregular from karst processes (Parker, 1992), the actual ground surface topography at the site is extremely flat, with elevation throughout the study area varying by less than one meter (Kruse *et al.*, 2006). An absence of surficial features is typical of covered karst environments, where topographic irregularities from karst subsidence are masked by the soil mantle (Parker, 1992).

1.6.2 Previous Studies & Site Characterization

As discussed in Section 1.3, geophysical methods are well-established for coarse resolution sinkhole detection, though work is still being undertaken in this study area to better understand the relationship that conduits have in regulating groundwater in karst aquifers (Bumpus & Kruse, 2014). Ground-penetrating radar (GPR) and resistivity methods have been used to successfully image shallow collapse conduits (Kruse *et al.*, 2006) and closely spaced electrical resistivity tomography (ERT) profiles can resolve sinkhole locations and provide an estimate of cavity volume given favorable site conditions, which include increased ground moisture content and electrical conductivity (Youssef *et al.*, 2012; Ungureanu *et al.*, 2017).

Combined, GPR and ERT have the ability to resolve the structure of clay confining layers at the base of large sinkholes. Kruse *et al.* (2006) were able to consistently image a 15 m diameter sinkhole at this site using the combination of 2D ERT with 0.5 m and 1 m electrode spacing and a 3D GPR survey. While their resistivity survey was unable to clearly resolve meter-scale conduits within the main sinkhole, GPR showed the most promise for imaging finer areas of interest within a larger depression. In a similar karst environment, Youssef *et al.* (2012) resolved a 3-6 m diameter sinkhole using 1 m electrode spacing in a dipole-dipole array. It is therefore clear that resistivity anomalies smaller than the electrode spacing can not be resolved using the ERT method, but the level of success in detection is highly dependent on site conditions and survey geometry (Zhou *et al.*, 2002; Youssef *et al.*, 2012).

Another combination that has been utilized successfully in karst environments is ERT constrained with the active multichannel analysis of surface waves (MASW) seismic method. Bansah & Anderson (2018) showed the potential of this multimethod

approach for mapping the topography of karst bedrock covered by soil. At the GeoPark site, Park & Taylor (2010) combined four 2D MASW survey lines with inverse-distance-weighted interpolation to form a pseudo-3D data cube of shear wave velocities. Shear wave velocity anomalies detected in the 3D interpolation were suspected as sinkhole locations because they matched closely with a previously-constructed geologic cross section (Parker, 1992); however, the authors recommend a more densely spaced receiver geometry to more thoroughly characterize subsurface heterogeneities. A more recent study by Bumpus & Kruse (2014) conducted a long-duration high-resolution self-potential survey of the GeoPark site in order to better understand the relationship between self-potential and aquifer recharge rates through collapse conduits. The authors concluded that the position of the self-potential reference electrode is critical for systematic correction and the requirement for several self-potential reference locations within closed loops. Self-potential data presented in Section B.1 of this study were also used by Grobbe & Barde-Cabusson (2019) to characterize preferential downward groundwater infiltration through a sinkhole and conduit system at the GeoPark. Passive self-potential methods are sensitive to naturally occurring differences in electrical potential between two electrodes. Changes in the potential field are used to determine groundwater flow direction, and in general a negative self-potential anomaly corresponds to gravity-driven flow moving away from the surface as in a drain or collapse conduit (Bumpus & Kruse, 2014; Grobbe & Barde-Cabusson, 2019; Barde-Cabusson *et al.*, 2020).

Each geophysical method discussed above provides a unique perspective of the subsurface and can often complement other characterization methods. An example of this is the use of resistivity and ground-penetrating radar to investigate layer con-

trasts in karst structure. A useful characteristic of conduit formation for geophysical investigation is the presence of raveling, or layered sediments that fill the space left by a sinkhole depression. GPR is the most commonly-used geophysical method for sinkhole detection due to the ability of the method to resolve these layered and weathered clay-rich sediments forming at the conduit base (Kruse *et al.*, 2006). As discussed in Kiflu *et al.* (2016), electrical resistivity methods are sensitive to lithology, saturation and pore water composition. Resistivity methods are most useful when imaging karst environments with a significant variation in conductivity between the carbonate layer and overlying sediments (Zhou *et al.*, 2002; Bansah & Anderson, 2018).

Active seismic surface wave methods such as MASW are sensitive to ground stiffness and density through shear wave velocity. Ground stiffness distribution is often an important subsurface property for the initial detection and characterization of large sinkholes in developed areas like Florida. However, resolving smaller, localized anomalies within karst environments (including voids, cavities, and conduits) challenges the resolution limits of common geophysical methods, including resistivity, GPR and active seismic, despite successes in identifying suspected large-scale sinkhole locations (e.g., Park & Taylor, 2010). The 3D MASW survey used to characterize a sinkhole roughly 50 ft in diameter at the USF GeoPark site by Park & Taylor (2010) consisted of four 2D MASW lines dividing an area 120 ft square. A 24-station land streamer with a sledge hammer source used 4.5 Hz geophones with 5 ft spacing. The fundamental mode surface wave dispersion curves had frequencies between 10 and 70 Hz.

Sloan *et al.* (2015) used active-source backscatter analysis of surface waves (BASW) to detect voids in the form of illicit subsurface tunnels. They employed a weight drop

with 40 and 4.5 Hz geophones (to collect body waves and surface waves, respectively) on a 24-station land streamer with an aperture of 1.22 m, similar to the GeoPark MASW study by Park & Taylor (2010). A parallel investigation into tunnel detection utilizing the MASW method was attempted in a field test in a dry desert environment, but was abandoned when it was discovered the shear wave velocity structure of the site and higher mode surface waves obscured the target of interest. The authors suggest that shallow subsurface voids can be detected using diffractions and back-scattered surface waves through the BASW method, but that tunnel detection in a noisy and less-than-ideal operational environment is a considerable and ongoing challenge for geophysical methods. Most importantly, the active-source methods discussed here are independent of time and only give an instantaneous snapshot of the subsurface; passive methods such as seismic interferometry enable the monitoring of structural changes over time.

1.7 Seismic Interferometry

1.7.1 Theory

As with other applied geophysical methods for sinkhole detection, the theory underlying the seismic interferometry method is well-understood. Interferometry is the study of interference phenomena between pairs of signals in order to obtain information from the differences between them (Curtis *et al.*, 2006). Seismic interferometry is thus the application of interference to estimate wave properties between stations.

The principal mathematical operation used in seismic interferometry is crosscorrelation. The convolution operation could also be used, as crosscorrelation is simply convolution with one of the signals time-reversed.

Two steps are required to fulfill the seismic interferometry operation: Crosscorrelation of a random isotropic wavefield recorded at a pair of arbitrarily-located receivers followed by the summation, or stacking, of the resulting correlograms. Stacking integrates over all actual sources and results in the recovery of the impulse response (Green's function) from a virtual source imagined to be at the location of one of the two receivers (Shapiro *et al.*, 2005; Curtis *et al.*, 2006; Bensen *et al.*, 2008). In a 3D elastic earth model, sources must surround the area of investigation except along reflecting boundaries such as the surface of the Earth (Wapenaar & Fokkema, 2006). In short, correlation turns a seismic receiver into a virtual seismic source.

1.7.2 Development

Claerbout's conjecture states that the crosscorrelation of noise traces recorded at two receivers in three-dimensional heterogeneous media gives the impulse response that would be observed at one of the receiver locations as if there was a source at the other location (Claerbout, 1968). Wapenaar (2004) proved the generalization of Claerbout's conjecture for three-dimensional acoustic and elastodynamic media without making assumptions with respect to source locations, the heterogeneity of the media or diffusivity of the wavefield. For mutually uncorrelated noise sources, impulse response expressions for many noise sources simplify to a single crosscorrelation of noise recorded at a pair of receivers (Wapenaar & Fokkema, 2006).

Work by Campillo & Paul (2003) represents the first geophysical interferometric impulse response reconstruction using seismic noise. They correlated seismic coda waves from earthquakes to estimate inter-receiver Green's functions, successfully recovering the surface wave part of the impulse response. Shapiro & Campillo (2004) extracted coherent Rayleigh waves from ambient seismic noise using crosscorrelation

and stacking of random wavefields. Their findings suggested the first possibility of measuring broadband Rayleigh wave dispersion curves between any pair of seismic stations.

Curtis *et al.* (2006) further described the history and development of the seismic interferometry method and provide a high-level review of specific techniques, presenting several applications of the method. Included are the detection of temporal changes in media following seismic events, surface wave velocity mapping using oceanic microseisms, and estimating building responses for earthquake preparedness. On a smaller scale, Halliday *et al.* (2008) used passive seismic interferometry to successfully extract surface waves traveling between two receivers in a suburban setting using automobile noise as a source. Although the automobile noise source was controlled in their experiment, they show the potential for Green's function estimation using a passive source in a similar frequency band to the 5-30 Hz band used in this research. Their findings indicated that even inter-receiver scattered surface waves can be estimated using interferometry in areas with strong near-surface heterogeneity, as can occur in karst environments. Draganov & Ruigrok (2014) presented the current state of passive seismic interferometry theory as it relates to subsurface imaging, including a generalized workflow and assumptions for Green's function retrieval through virtual shot gathers. I implement portions of this workflow to process ambient seismic noise for tomographic inversion.

1.8 Ambient Noise Tomography

Ambient noise tomography is an application of seismic interferometry in which the fundamental mode surface wave is extracted from ambient seismic noise in the absence of an impulsive active source. Studies have also investigated the feasibility of

retrieving surface wave overtones to improve depth resolution and reduce uncertainty (Kimman & Trampert, 2010). Surface waves are extremely dispersive, meaning that their velocity varies as a function of the wave's period or frequency. Surface wave dispersion makes it possible to create tomographic inversions from group and phase velocities. Ambient noise tomography generally involves two steps: An intermediate step consisting of a two-dimensional tomography map or model at each frequency generated from interstation group or phase velocities, and a one-dimensional shear wave velocity (Vs) model created by inversion of a dispersion curve extracted from each point in space. The dispersion curve contains velocity information for all frequencies at each pixel within the boundary of the passive array.

Studies at the regional scale (average interstation spacing greater than 50 km) dominate the literature. Shapiro *et al.* (2005) and Sabra *et al.* (2005) were the first applications of ambient noise tomography, both in California on the regional scale. Following their initial efforts, ambient noise tomography studies have been undertaken across Europe (Yang *et al.*, 2007; Stehly *et al.*, 2009; Guerin *et al.*, 2019), the United States (Moschetti *et al.*, 2007; Bensen *et al.*, 2008; Lin *et al.*, 2008), New Zealand (Lin *et al.*, 2007) and China (Zheng *et al.*, 2008). Global-scale ambient noise tomography has also been used to investigate the deep internal structure of the Earth (Nishida *et al.*, 2009).

Only a handful of previous studies using ambient noise tomography have been performed at the local scale, which I define as average interstation spacing between 1 and 50 km. Brenguier *et al.* (2007) were the first to use ambient noise tomography at the local scale, successfully imaging the velocity structure of a 10 km diameter volcano caldera using an array with interstation spacing between 10 and 35 km. A more recent

near-surface study (Mordret *et al.*, 2013) with interstation spacing ranging from 1 to 1.5 km successfully extracted group velocity maps at frequencies below 2 Hz using the MSNoise software package (Lecocq *et al.*, 2014). This study also utilizes the MSNoise package, though the array in used for this research has an average interstation spacing less than 100 m, which is considerably shorter than previous applications of local scale ambient noise tomography and is designed for small-scale site characterization.

CHAPTER 2:

GEOPHYSICAL DATASETS & ACQUISITION

The main focus of this research is ambient noise tomography, but additional complementary geophysical methods were used to constrain and validate the main results.

A team of researchers (Dylan Mikesell, Zongbo Xu and Thomas Otheim from Boise State University, Niels Grobbe and Stéphanie Barde-Cabusson from the University of Hawaii at Manoa, and Sarah Kruse and Tonian Robinson from the University of South Florida) collected a series of complementary geophysical datasets to validate and constrain the ambient noise tomography created from the passive nodal seismic deployment. The data collection campaign took place during the spring of 2019 at the GeoPark study area. These complementary datasets include both active source (2D resistivity, common-offset GPR) and passive source methods (self-potential). Figure 2.1 displays an overview of the different survey geometries and sampling locations for each method in this study.

2.1 Self-potential

Niels Grobbe and Stéphanie Barde-Cabusson (University of Hawaii at Manoa) collected 438 self-potential measurements over the study area. The set of measurements (Figure 2.1) had an average spacing of 10 m north to south and 20 m east to west. Prior to this study, these self-potential data were used by Grobbe & Barde-Cabusson

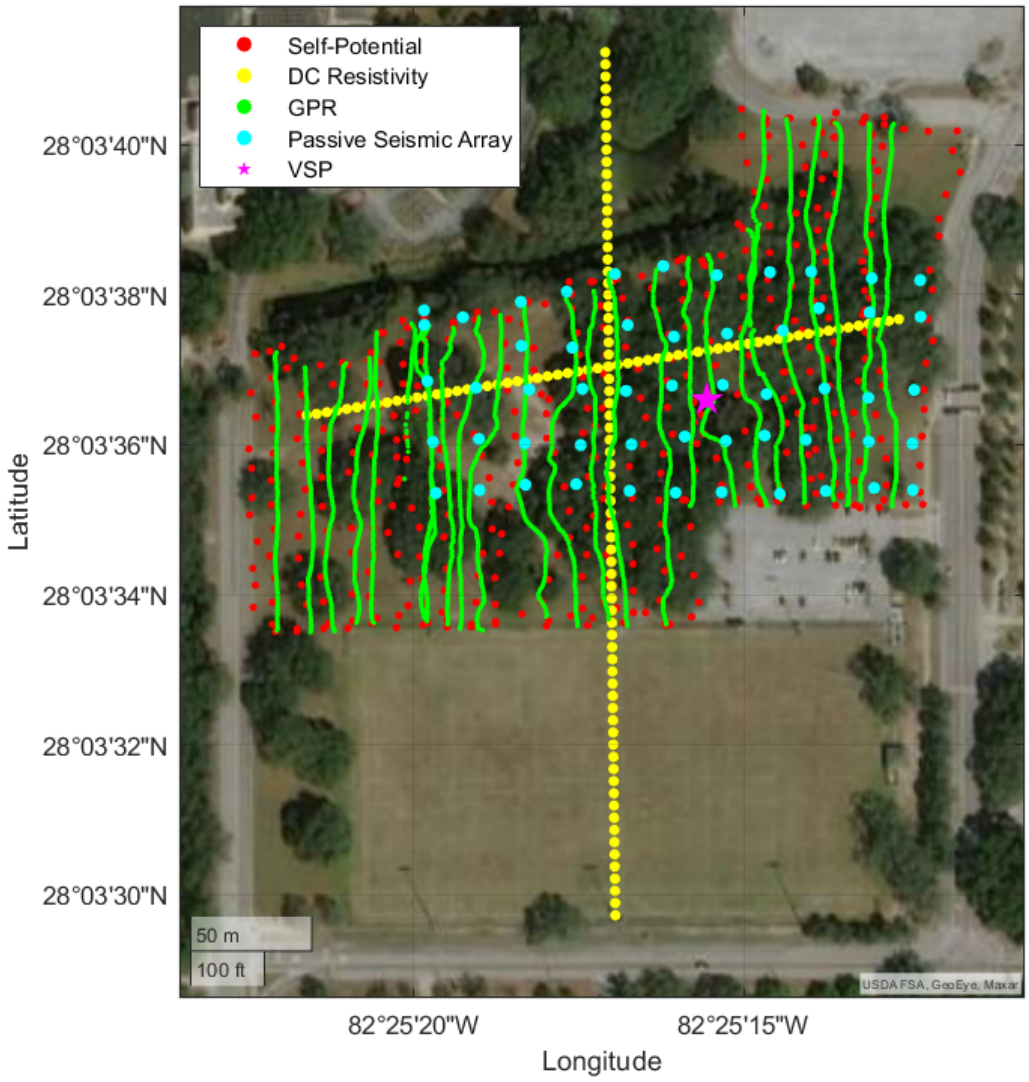

Figure 2.1 Overview and acquisition geometry of multiphysical survey conducted at the GeoPark study area in the spring of 2019.

(2019) to characterize preferential downward groundwater infiltration through a sinkhole and conduit system at the GeoPark.

2.2 2D Electrical Resistivity Tomography

Using an IRIS Syscal Pro multinode resistivity system, Dylan Mikesell, Thomas Otheim, and Zongbo Xu (Boise State University) designed and performed a 2D resistivity survey using a dipole-dipole survey geometry. Electrode spacing was 3.33 m. The survey consisted of two roughly perpendicular lines bisecting the study area and oriented north to south and east to west (Figure 2.1). The north-south line is 365 m in length and the east-west line 278 m in length.

2.3 Ground Penetrating Radar

A ground penetrating radar (GPR) survey was conducted over the GeoPark study area consisting of 24 north-south lines. GPR trace collection was every 0.02 m. The GPR lines are roughly parallel to the north-south resistivity line and cover an area similar to that of the self-potential survey (Figure 2.1). The GPR survey was performed using 250 Hz antennas with 0.31 m common-offset spacing.

Surface elevation across the site increases uniformly by 10 cm from south to north (Kruse *et al.*, 2006) and this variation was neglected in GPR data processing.

2.4 Seismic Interferometry

The ambient seismic data used for seismic interferometry was gathered using a 54-element nodal array (1C and 3C sensors) recorded over 20 days within an area of approximately 0.02 km^2. The ambient noise record consisted primarily of surface waves generated by vehicle traffic. The noise itself was non-isotropic due to the inhomogeneous distribution of roads encompassing the survey site (Figure 2.2). Figure 2.3

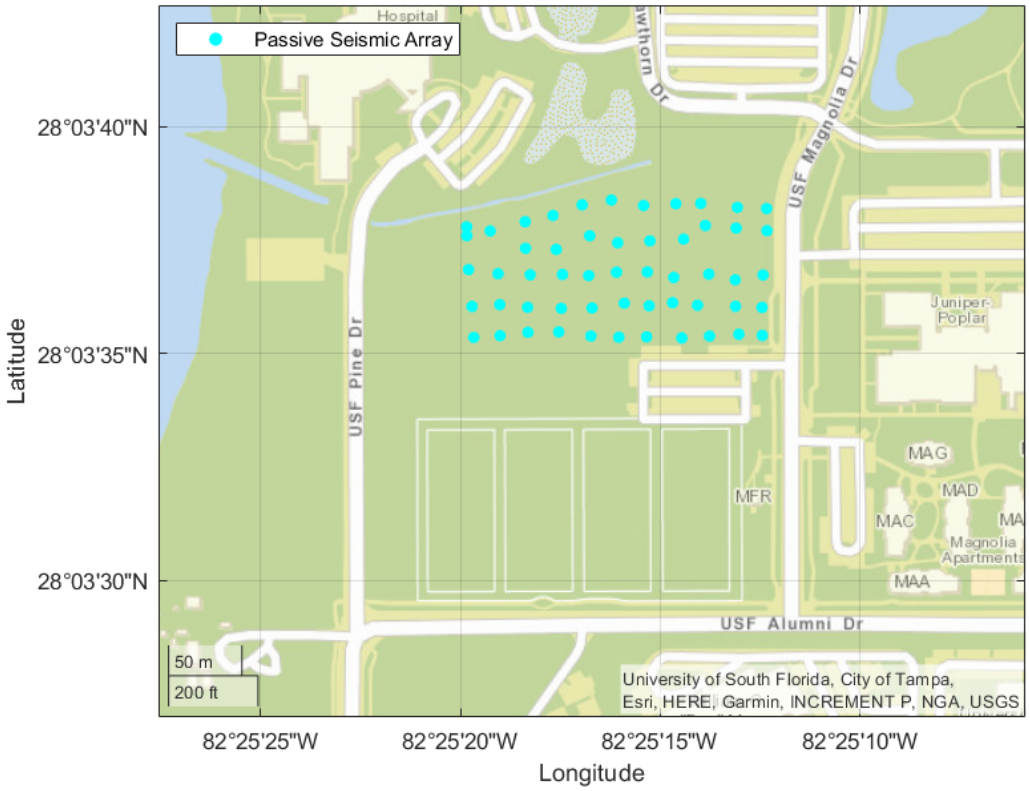

Figure 2.2 Road layout around the USF GeoPark illustrating the potential for an inhomogenous noise source distribution in relation to the passive seismic array.

illustrates the distribution of interstation distances in the passive seismic array. At 5 Hz, the average interstation distance satisfies the two-wavelength criteria described by Mordret *et al.* (2013).

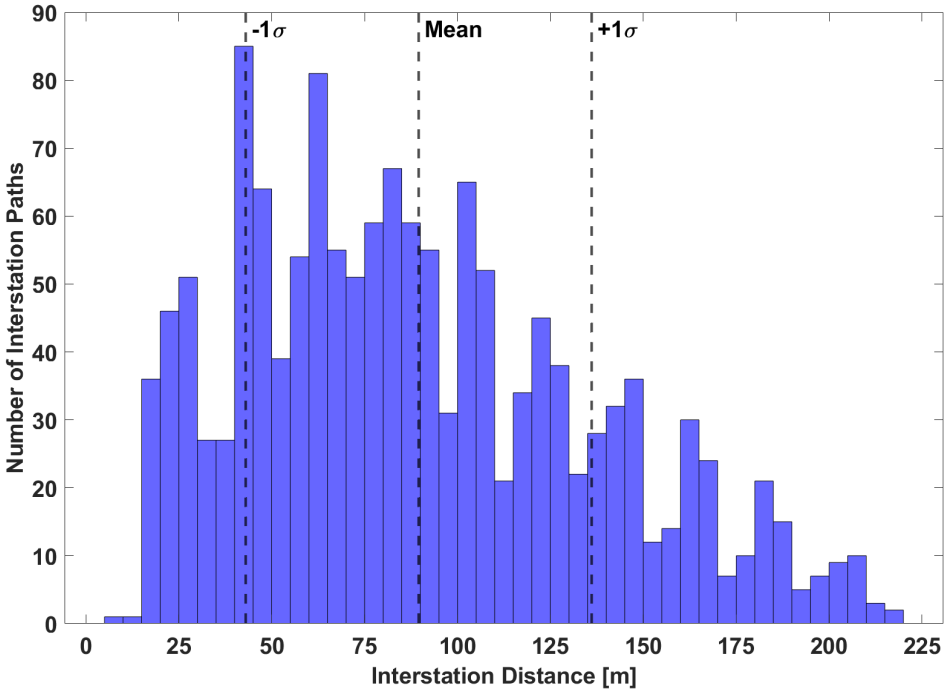

Figure 2.3 Distribution of passive seismic array interstation paths as a function of interstation distance.

CHAPTER 3:

COMPLEMENTARY DATASETS

3.1 Self-potential

I process the self-potential data for reference and loop/closure corrections using the framework outlined by Barde-Cabusson *et al.* (2020), using a biharmonic interpolation of the complete dataset to create a two-dimensional surface.

3.2 2D Electrical Resistivity Tomography

I process the resistivity data and perform a tomographic inversion on the N-S and E-W resistivity lines using the finite-difference method with the Geotomo RES2DINV software package. Tomography is neglected in the inversion due to minimal elevation variation at the survey site. Model block spacing is 3.33 m, following the electrode spacing. The convergence limit is set to 5% of the relative change in RMS error between iterations.

3.3 Ground Penetrating Radar

Tonian Robinson from the University of South Florida processed the GPR lines using the Reflexw software package by manually picking the strongest reflector horizon in each of 24 lines. These reflectors were combined and interpolated using a 3D mesh grid with 1 m square grid spacing to create the reflector surface.

CHAPTER 4:

SEISMIC INTERFEROMETRY

4.1 Preprocessing

I preprocess the raw ambient seismic data with the objective to improve the signal-to-noise ratio (SNR) of the resulting cross correlations and minimize the effect of transient, high-amplitude signals by attempting to create a symmetric crosscorrelation (Bensen *et al.*, 2008; Mordret *et al.*, 2013). The preprocessing steps include:

1. removal of the geophone instrument response,
2. bandpass filtering of the ambient noise between 2 and 30 Hz,
3. clipping amplitudes larger than the root mean square of the signal,
4. brutal spectral whitening of the signal (i.e. setting the relative amplitude of all frequencies to 1.0).

4.2 Daily crosscorrelations

I recover strong Rayleigh wave signals while minimizing noisy spikes in the time domain that result from whitening in the frequency domain. The resulting waveforms are asymmetric due to an inhomogenous source distribution in the study area. There is energy propagating in negative time but it is much lower in amplitude than energy in the positive time correlation.

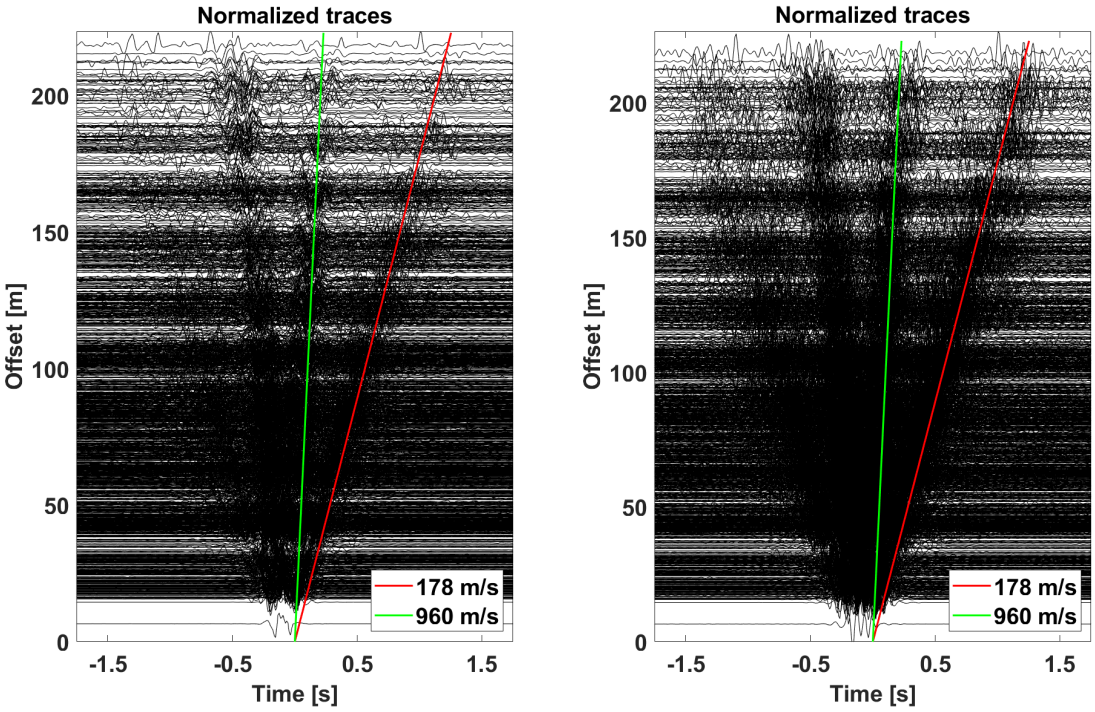

Figure 4.1 Interstation crosscorrelation functions in the GeoPark array bandpass filtered from 2-30 Hz (left) and 10-20 Hz (right). Move out velocities are for surface waves (178 m/s) and body waves (960 m/s).

Figure 4.1 shows a virtual shot record demonstrating the non-isotropic source distribution of positive and negative time correlation functions between stations in the GeoPark passive array. The correlation functions have been bandpass filtered between 2-30 Hz and sorted by increasing interstation distance. The virtual shot record on the right is further filtered to 10-20 Hz for clarity.

I approximate daily Green's functions between station pairs by crosscorrelating and stacking cross correlations of short time windows. The ZZ component correlations (Z-vertical force direction and response direction) are used in my analysis. I utilize Welch's method to divide ambient seismic records into short overlapping time windows prior to correlation and stacking through implementation of the the MSNoise software (Lecocq *et al.*, 2014). Correlating and stacking overlapping small windows (36-72 times the longest period) converges more quickly to a reliable correlation function than other preprocessing methods (Seats *et al.*, 2012). With my lowest frequency of 2 Hz corresponding to a period of 0.5 seconds, I choose a 60 sec time window to prevent aliasing of lower frequencies along with a 75% overlap between windows. Linear stacking of all correlation windows in a single day result in 28,620 daily interstation crosscorrelations over the 20-day recording period. The final daily correlation output is trimmed to ± 10 seconds in length.

4.3 Stacking

I stack the daily crosscorrelations with the nonlinear phase-weighting method of Schimmel & Paulssen (1997) where every trace in the linear stack is weighted by the coherency, or the similarity between traces, of its instantaneous phases. The phase stack is time-dependent and strengthens weaker coherent signals by attenuating incoherent noise. The primary benefit of a phase-weighted stacking method

over a linear stacking method is that while some distortion is always expected from a nonlinear method, the coherent signals will experience minimal distortion as they should be stationary in phase over the entire waveform. Thus, waveform distortion with this method does not depend on amplitude, but instead on coherency.

Increasing the power of the phase stacking method from 1 (a simple linear stack) to 2 (squared phase) increases the signal-to-noise ratio. Coherency in the phase stack is smoothed by averaging the measurements over a time-gate (Schimmel & Paulssen, 1997). I use a squared phase (i.e. a power=2) with a time-gate of 0.05 s. This produces a single crosscorrelation for each of the 1431 interstation pairs, resulting in a virtual shot with coherent surface wave energy moving through the survey area (Figure 4.1). Prior to surface wave group velocity estimation, I symmetrize the crosscorrelations (i.e. averaging the acasual and causal sides of the correlation function).

CHAPTER 5:

SEISMIC TOMOGRAPHY & VS INVERSION

I perform ambient noise tomography following the seismic interferometry processing steps described in Chapter 4 using the general flowchart in Figure 5.1. I use the Python-based MSNoise software package (Lecocq *et al.*, 2014) with the MSNoise-TOMO plugin for surface wave tomography. The MSNoise code was designed for regional- to global-scale applications sampling the lower crust at low frequencies or long periods, with correspondingly faster velocities. I optimized the MSNoise code for near-surface ambient noise tomography applications, particularly small scale (less than 1 km) interstation spacing, high frequencies (or short periods) and the slower velocities found in near-surface sediments.

5.1 Group velocity estimation

I apply two-dimensional Frequency-Time Analysis (FTAN) (Levshin *et al.*, 1972) to the stacked symmetric crosscorrelations in order to determine interstation group velocities. FTAN involves a Fourier transform of detrended time series seismic waveforms into the frequency domain, followed by a phase correction for the instrument phase response. Narrowband filtering by Gaussian filters with varying central frequencies results in a normalized frequency-group velocity amplitude map as in Levshin *et al.* (1992). The fundamental mode surface wave dispersion curve is estimated

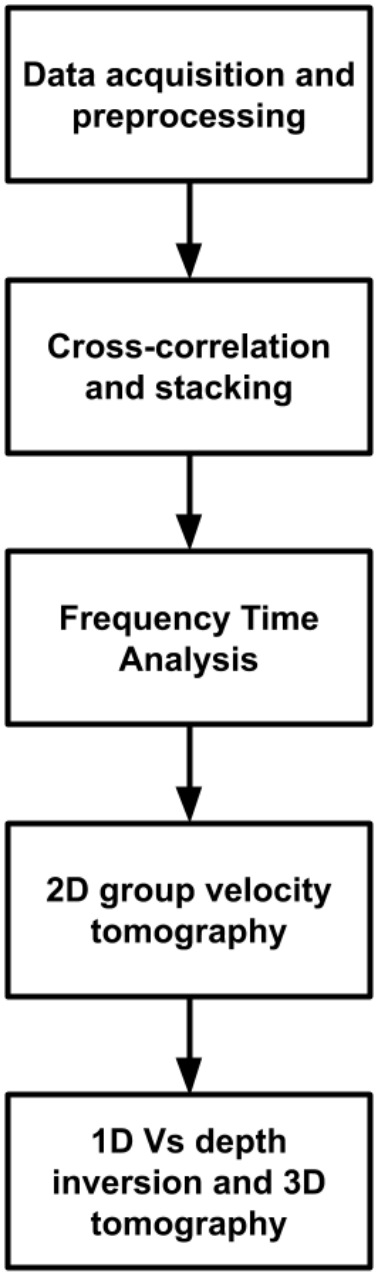

Figure 5.1 Generalized processing flowchart to perform ambient noise tomography.

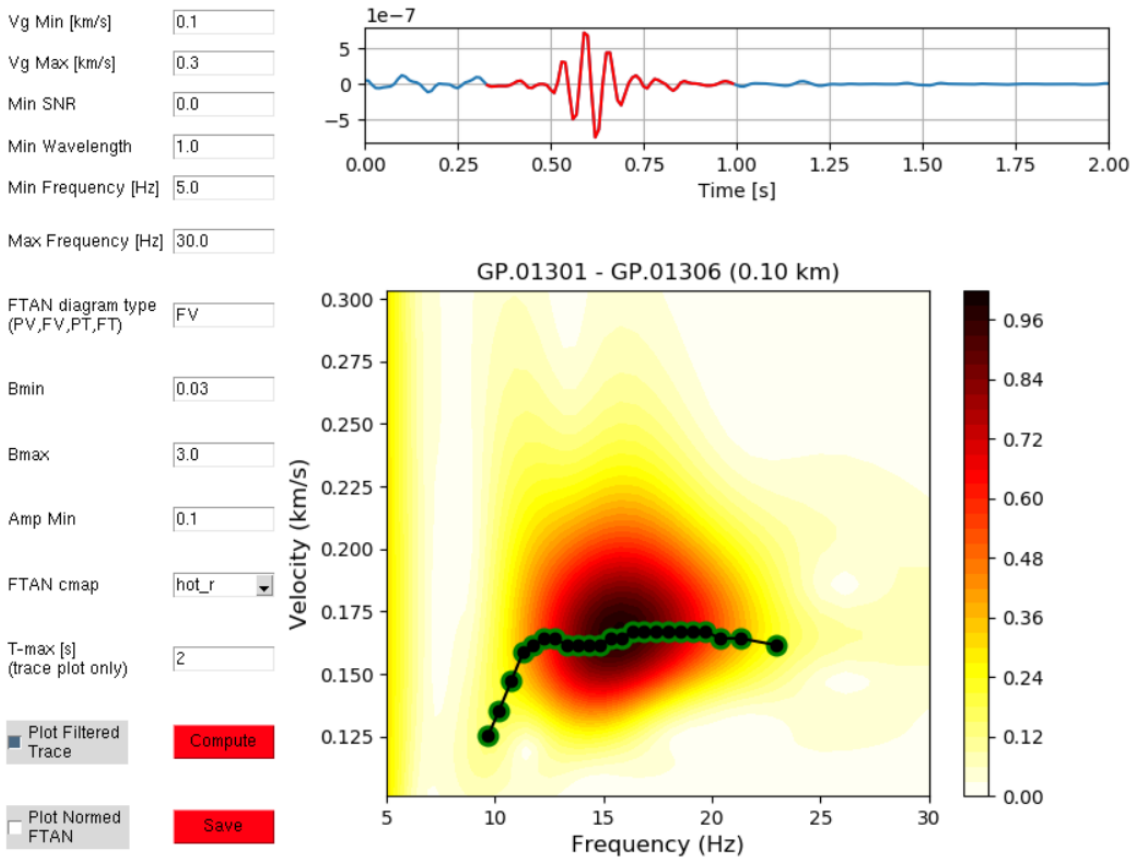

Figure 5.2 Interactive Frequency-Time Analysis tool to estimate group velocities dispersion curves from the MSNoise-tomo plugin.

through automatic picking of the maximum amplitude at each frequency. I use the interactive FTAN tool (Figure 5.2) in the MSNoise-TOMO plugin to estimate group velocities of the stacked correlation functions between 5-30 Hz at 1 Hz intervals. I use a variable-width Gaussian bandpass filter from 0.03-3 Hz to create the frequency-group velocity amplitude map. I constrain the group velocity between 0.1-0.3 km/s to isolate the group velocity of the fundamental mode surface wave in near-surface sediment.

5.2 2D Group Velocity Tomography

Following estimation of the group velocity dispersion curve, I use straight-ray 2D tomography from Barmin *et al.* (2001) to invert for 2D group velocity maps. This method has shown promising results in previous ambient noise tomography studies (e.g., Shapiro *et al.*, 2005; Brenguier *et al.*, 2007; Lin *et al.*, 2008; Mordret *et al.*, 2013). The FTAN tool provides dispersion curves as inputs for the 2D tomography, resulting in group velocity maps at each of 26 frequencies. The tomographic inversion minimizes the following objective function:

$$S(m) = (G(m) - d)^T C_d^{-1}(G(m) - d) + \alpha||F(m)||^2 + \beta||H(m)||^2,$$

where

$$F(m)(x) = m(x) - \int_S K(x, x')m(x')dx'$$

with

$$K(x, x') = A\ exp\ \left(\frac{-|x - x'|^2}{2\sigma^2}\right)$$

and

$$H(m) = exp(-\lambda\rho(x)).$$

The first term is the deviation of the predicted model from the observed data. $F(m)$ represents the Gaussian spatial smoothing condition, with smoothing strength α and correlation length σ in meters.

As the final term in the objective function, $H(m)$ penalizes the weighted norm of the model by placing a damping constraint on the amplitude of the perturbations based on local raypath density $\rho(x)$, containing damping strength β and constant parameter λ.

I determine the smoothing and damping parameters used in the inversion by analyzing the change in variance reduction that occurs by varying the parameters α, β, σ and λ. As in Mordret *et al.* (2013), the damping parameter β (and by extension, constant parameter λ) has no influence on the inversion due to dense and homogeneous raypath coverage. The raypath density of the GeoPark passive array is greater than 20 rays per pixel (Figure 5.5), resulting in satisfactory raypath coverage in each cell to negate the damping constraint controlling raypath density weighting entirely. Thus, β and λ are set to zero in the 2D group velocity tomography inversions. σ is set to 10 m using a similar variance reduction analysis method, which is approximately twice the width of the cells in the tomographic inversion. The only parameter strongly affecting the inversion results is the smoothing parameter α, illustrated by the variance reduction plot in Figure 5.3. Small values of the Gaussian spatial smoothing parameter α result in higher variance reduction, but the tomography becomes dominated by small-scale features related to station geometry and path density (Figure 5.4). Increasing the smoothing parameter ($\alpha \geq 10$) yields an oversmoothed model. α is set to a constant value of 1 for all frequencies. I select smoothing and damping parameters that provide relatively smooth models with high variance reduction.

The final group velocity inversion is performed with a two-step inversion as in Moschetti *et al.* (2007) and Mordret *et al.* (2013). The bounds for the inversion are

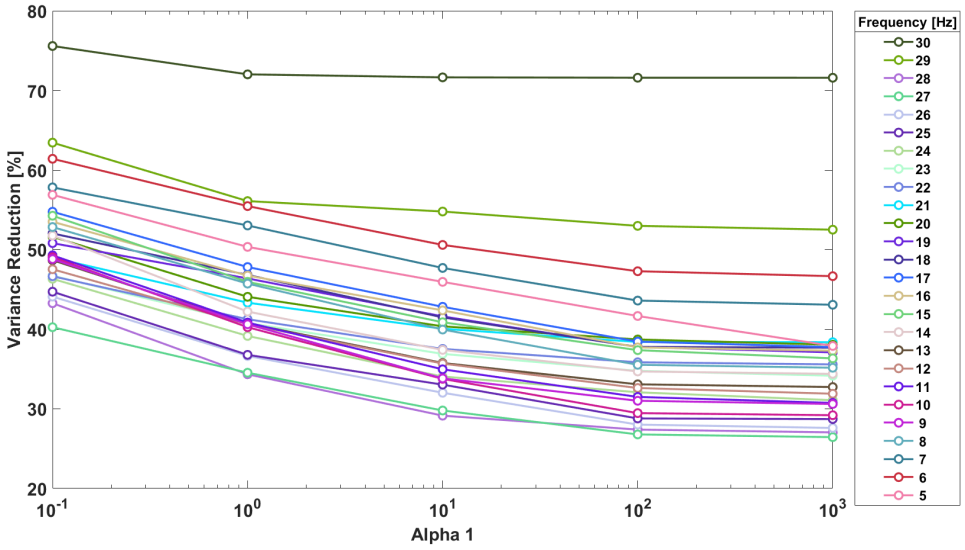

Figure 5.3 Variance reduction as a function of the α (Gaussian smoothing) parameter for 5-30 Hz. $\alpha = 1$ is chosen as the final value for the smoothing parameter.

denoted by the zero ray density contour shown by the black outline in Figure 5.4) with cell dimensions of 0.00005 degrees in both the x and y directions. This corresponds approximately 5.5 m at the geographic location of the GeoPark study area.

The first step of the inversion produces an initial group velocity model using the step 1 parameters in Table 5.1. The interstation travel times are computed for all station pairs and compared to the observed travel times. Any data points with a travel time difference greater than three standard deviations are considered an outlier and rejected. The second step uses the updated data set with step 2 parameters to redo the inversion with the outliers removed. I hold the parameters constant for each inversion step (Table 5.1).

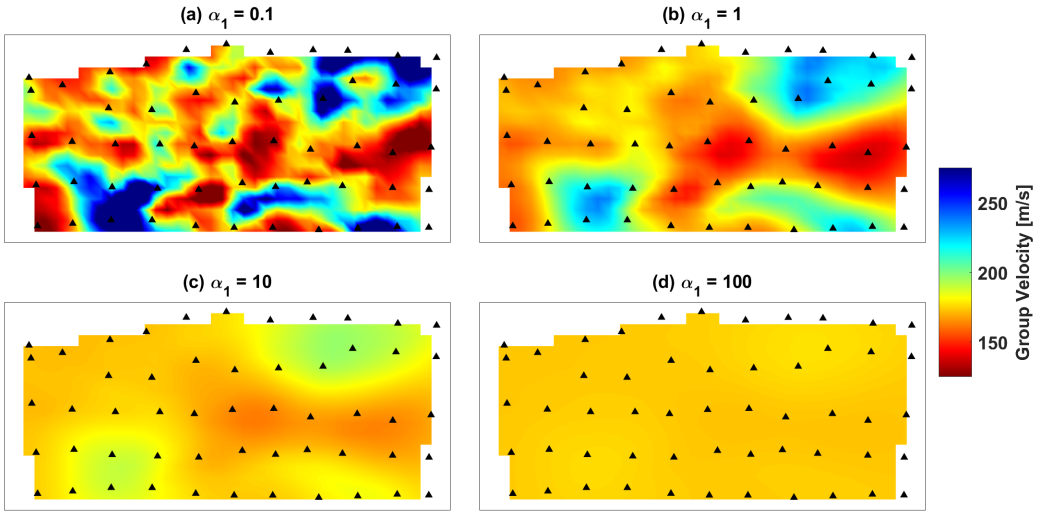

Figure 5.4 2D group velocity tomography maps at 15 Hz showing the effect of changing the alpha regularization parameter. Oversmoothing occurs in (c) and (d).

Table 5.1 Final regularization parameters for 2D tomographic group velocity inversion. α and σ are smoothing parameters and β and λ are damping parameters.

Parameter	Value
α_1	1.0
β_1	0
λ_1	0
σ_1	0.01
α_2	1.0
β_2	0
λ_2	0
σ_2	0.01

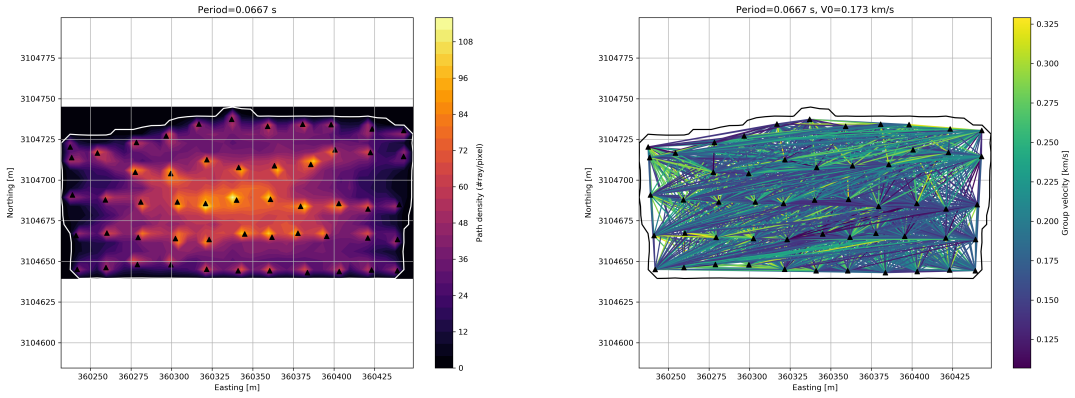

Figure 5.5 2D tomography path density (rays per pixel) at 15 Hz (left) and 2D straight-ray tomography highlighting raypaths and corresponding group velocities at 15 Hz (right), an intermediate step in the MSNoise-TOMO inversion. High raypath coverage allows negation of the damping constraint β for path density weighting.

5.3 1D Vs Depth Inversion

I use the Markov chain Monte Carlo (MCMC) transdimensional Bayesian inversion implemented in the BayHunter package (Dreiling & Tilmann, 2019) to estimate the one-dimensional shear wave velocity structure with depth for each pixel in the GeoPark tomography.

I arrange the 2D group velocity tomography maps in increasing frequency after removing the 2D group velocity maps for 30 Hz and 29 Hz due to missing and poor data (Appendix A). I then extract the local dispersion curve for each of the 624 pixels of the 2D tomography grid, removing any missing data points. I perform the inversion on a pixel-wise basis for the vertical structure represented as a 1D depth-shear wave velocity curve. The model priors used in the inversion are shown in Table 5.2 with an acceptance rate range chosen to reflect findings by Bédard (2008).

The model priors are set to include a wide range; this was intended to reflect the suspected heterogeneity of a covered karst environment. The depth range for layer interfaces is restricted from the surface to a maximum of 250 m, the Vp/Vs ratio was from 1.4 to 2.1, the number of layers from 1 to 12 and the shear wave velocity from 0.1 to 4 km/s, or 100 to 4000 m/s. The inversion is performed with 30 chains to maintain independent search paths. Each chain completes 1.5 million iterations with a 2:1 ratio between the burn in and main or exploration phases. Chains that do not converge and return likelihoods smaller than the acceptance rate are labeled as outliers.

I solve for the shear wave velocity depth structure, the number of layers, the surface wave dispersion noise and the average Vp/Vs ratio. As Bayesian inversions are based on probability distributions for the parameters of the model instead of a single best model's misfit, the results of the shear wave are represented by a collection of models as in Dreiling *et al.* (2020).

The presence of a large model standard deviation at a given depth is an indication that there exists a sharp transition or boundary at that location. Bayesian inversion methods have difficulty choosing whether the shear wave velocity at the interface should increase or decrease, yielding a higher standard deviation as a percentage of shear wave velocity value. A boundary in a high shear wave velocity zone will have a higher standard deviation than a similar boundary that exists in a lower shear wave velocity zone.

I calculate the mean and the median shear wave velocity model from the 50,000 models containing the highest likelihood, sampled from non-outlier chains. I then use the mean shear wave velocity model to forward model a synthetic group velocity

dispersion curve at each pixel. This allows for direct comparison at depth between the input data (the group velocity dispersion curve) with the synthetic data for every pixel in the tomography grid.

I combine the results of the 1D inversion (624 geolocated 1D shear wave dispersion curves) into a 3D Vs cube. No interpolation is used on the shear wave velocity data, however the resulting Vs data cube is smoothed for purposes of analysis and presentation.

5.3.1 Boreholes

I curate and georeference borehole stratigraphy originally compiled by Parker (1992) for wells that intersect the ambient seismic array in order to constrain the depth to bedrock in the shear wave inversion. Five boreholes are contained within the study area, acquired by bucket-auger (BA) borings and standard penetration testing (SPT). Their locations are shown with respect to other site references in Figure 6.8 and the associated depth information is listed in Table 6.1.

Table 5.2 Regularization parameters and constraints for 1D shear wave velocity inversion. Velocities are shown in km/s.

Parameter	Value
Depth range	(0, 0.25)
Vp/Vs Ratio	(1.4, 2.1)
Number of layers	(1, 12)
Shear wave velocity	(0.1,4)
Surface wave dispersion noise σ	(1e-5, 0.001)
Iterations, burn in	100000
Iterations, main	50000
Acceptance (%)	(20, 25)
Max models	50000

CHAPTER 6:

RESULTS

The resulting models for self-potential, ground penetrating radar, 2D ambient noise tomography and 1D shear wave velocity inversion are plotted using a local coordinate system created using the mean location of the passive seismic stations. The benchmark reference for 0 m E 0 m N is 17N 360340 m E 3104700 m N.

6.1 Complementary Datasets

6.1.1 Resistivity

The 2D resistivity survey yields two lines of resistivity tomography, one crossing the study area from south to north and one west to east (Figure 6.1, top and bottom respectively). The resistivity tomography sections are vertically exaggerated to highlight near-surface features.

The south-north section exhibits variable high resistivity zones from the surface to a maximum depth of 10 m (Distance 130 m to 250 m). This high resistivity zone is not consistent over the length of the line, with lower resistivity values in the near surface towards the southern end of the line. From distance 250 m to 350 m, low resistivity features are present that break up the shallow horizontal structure above 10 m depth and breach the surface at 275 m and 325 m along the section. The west-east line has a high resistivity layer that is more consistent than the south-north line,

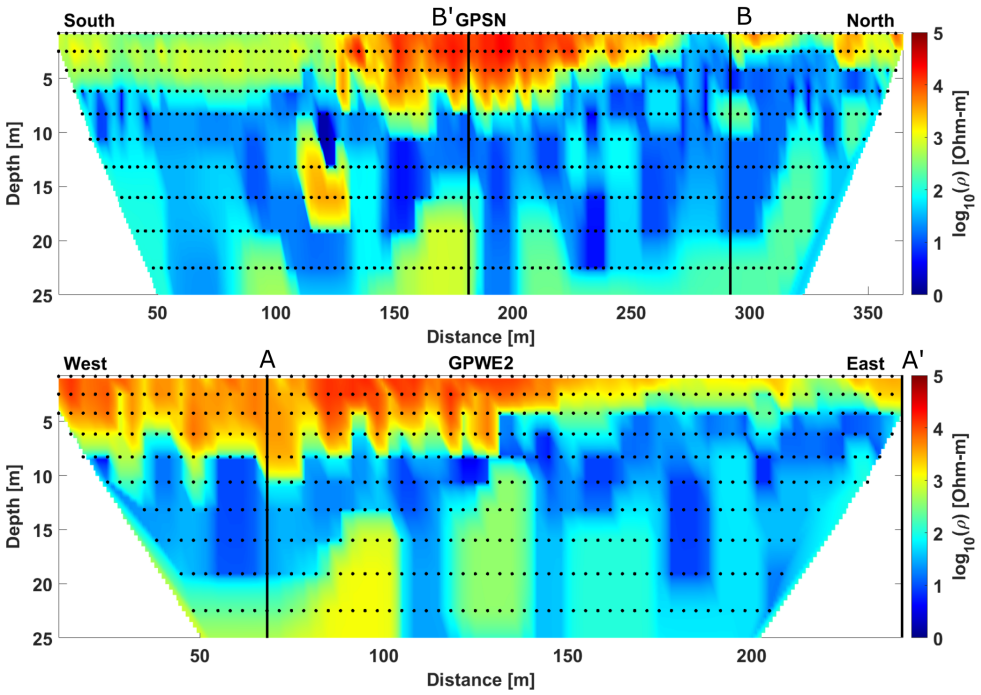

Figure 6.1 2D ERT survey of GeoPark site showing near-surface resistiv-ity structure, south-north line (top) and west-east line (bottom) with 5:1 vertical exaggeration. The vertical black bars correspond to the extent of the passive seismic array.

with a subsurface expression that gradually shallows from around 8 m depth in the west to less than 5 m depth in the eastern end of the section.

Both the south-north and west-east sections exhibit significant variability in the form of low resistivity vertical pipe features and point anomalies in the north and east sections at depths between 5 and 10 m. These features are visible between 200 and 350 m in the south-north section and between 140 and 250 m in the west-east section (Figure 6.1). Other low resistivity anomalies are present at depths greater than 10 m in other zones throughout both sections, though as shown in Figure 2.1 areas of the resistivity tomography that did not intersect the passive seismic array can not be constrained or correlated using ambient noise tomography.

The self potential data was collected and processed but does not add detail to the 2D ERT interpretation. The results of the self-potential method can be found in Appendix B.

6.1.2 Ground Penetrating Radar

The surface generated by the strongest radar reflector is shown in Figure 6.2. Depths of this horizon range from 1 to 5 m. There is a significant zone of depression near the center of the seismic array, with the deepest area approaching 5 m near 25 m E 10 m N. Other distinct depressions with depths near 4 m were located at the western and eastern edges of the survey area.

The central cavity feature is both deeper and more consolidated in structure than the depressions at the edges of the study area, which are somewhat divided and shallower. Around the central cavity, the horizon is much shallower (between 1 and 2 m) and consistent in depth, separating the deep feature from the depressions at the edges.

6.2 Ambient Noise Tomography

6.2.1 2D Tomography Maps

Selected results of the two-dimensional ambient noise group velocity tomographic inversion are shown in order of decreasing frequency corresponding to an increase in depth due to the dispersive nature of surface waves (Figures 6.3 - 6.7). As such, these frequency maps can be interpreted qualitatively as if they were slices in depth.

The set of tomography maps contain persistent features, particularly a slow group velocity zone at the center of the array. This slow zone generally extends through the array from east to west, with velocities ranging from 130 to near 200 m/s. Additional

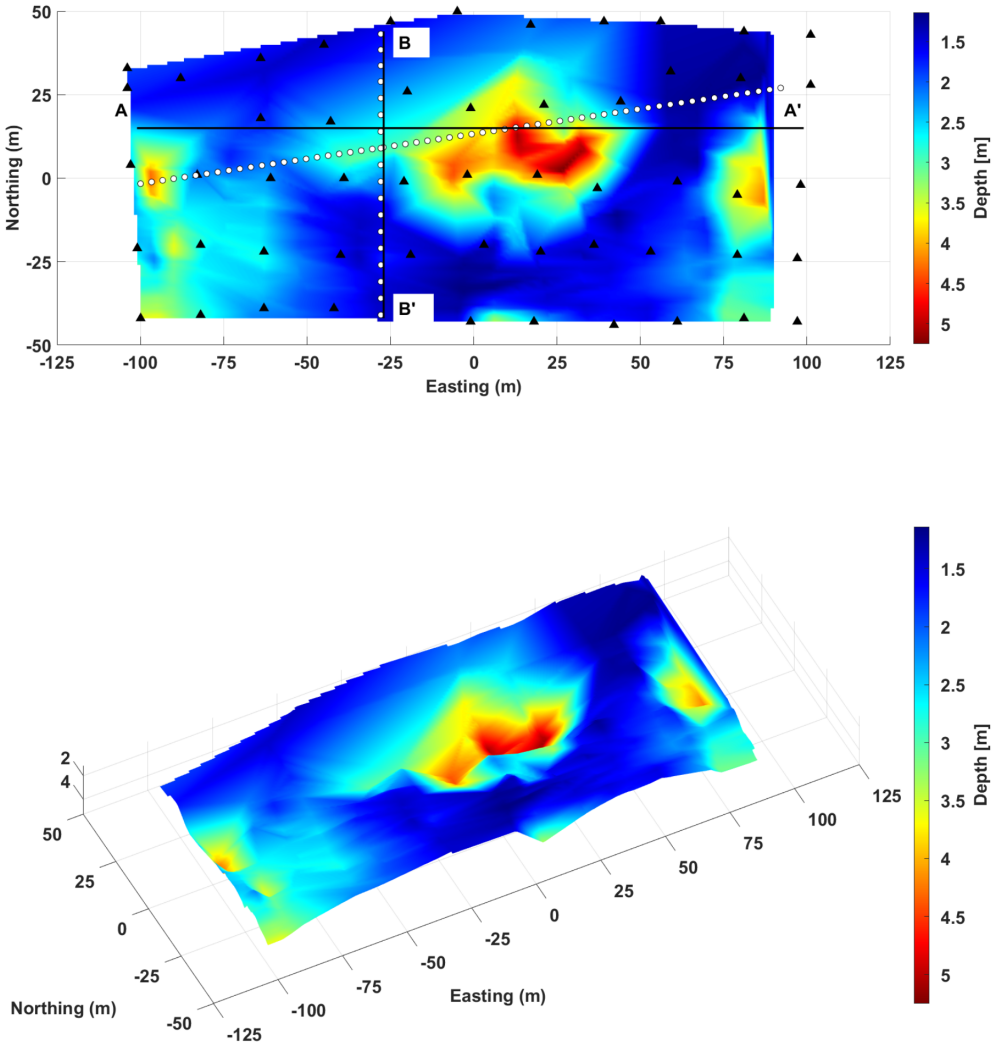

Figure 6.2 Strongest GPR reflector horizon with depths varying from 1-5 m. Map with superimposed ambient seismic array locations as black triangles, electrical resistivity lines as white circles and cross section reference locations A-A' and B-B' (top) and perspective view highlighting relief (bottom).

features consistent in the five maps shown in Figures 6.3 - 6.7 are a set of two zones with relatively higher velocities (220 to 270 m/s) in the southwest and northeast corners of the array.

The complete set of 2D tomography maps over all 26 frequency intervals is shown in Appendix A.

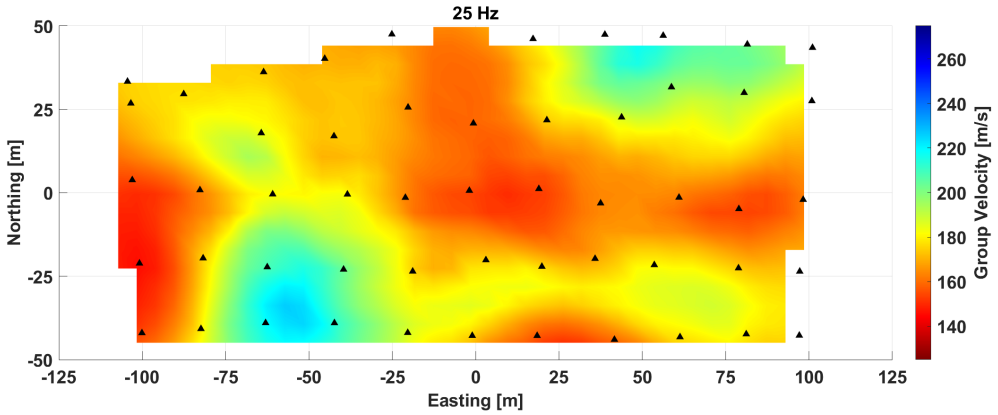

Figure 6.3 2D ambient noise tomography map at 25 Hz

6.2.2 1D Vs Depth Inversion

Borehole Stratigraphy

The boreholes intersecting the ambient seismic stations in the GeoPark study area are shown in Figure 6.8. Two in particular, SPT-1E and SPT-1F are located very close to the west-east ERT transect and the A-A' cross section. Table 6.1 contains the depth to bedrock information for the five boreholes shown.

3D Vs Tomography

The final 3D shear wave velocity model from the 1D shear wave inversion is shown as by the fence diagram in Figure 6.9. Note the orientation of the model space in relation to the cross sections A-A' bisecting the survey area west to east and B-B' south to north. A clear shear wave velocity boundary occurs in the model at depths of 5 m

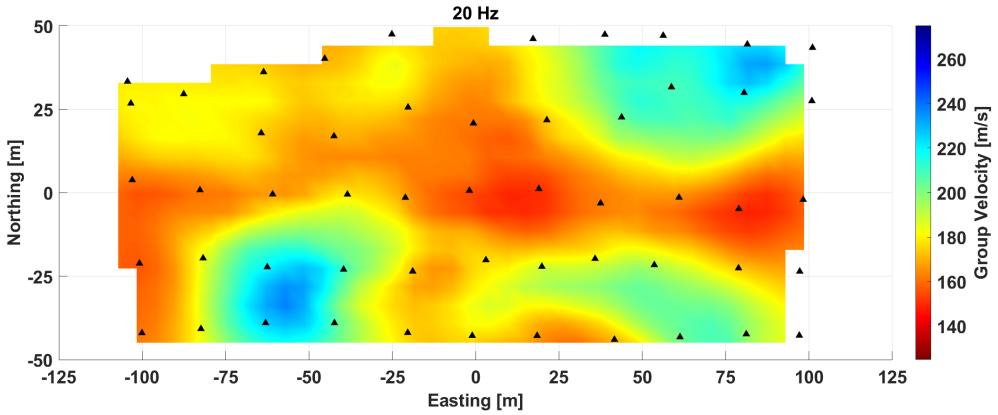

Figure 6.4 2D ambient noise tomography map at 20 Hz

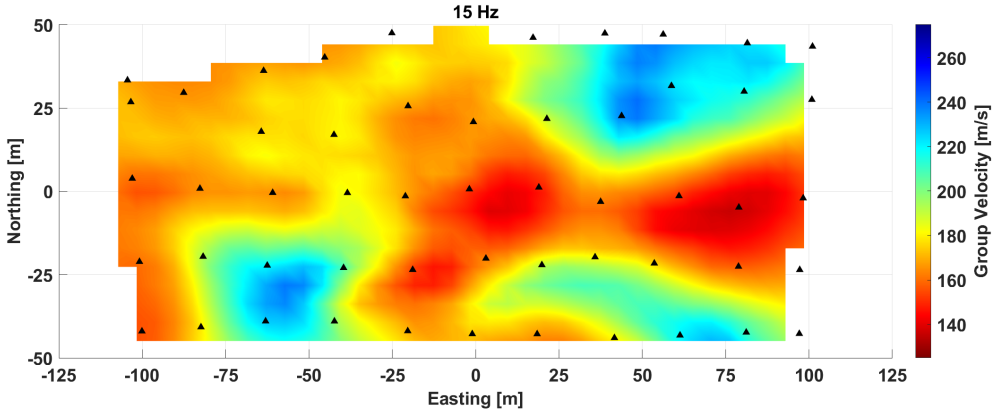

Figure 6.5 2D ambient noise tomography map at 15 Hz

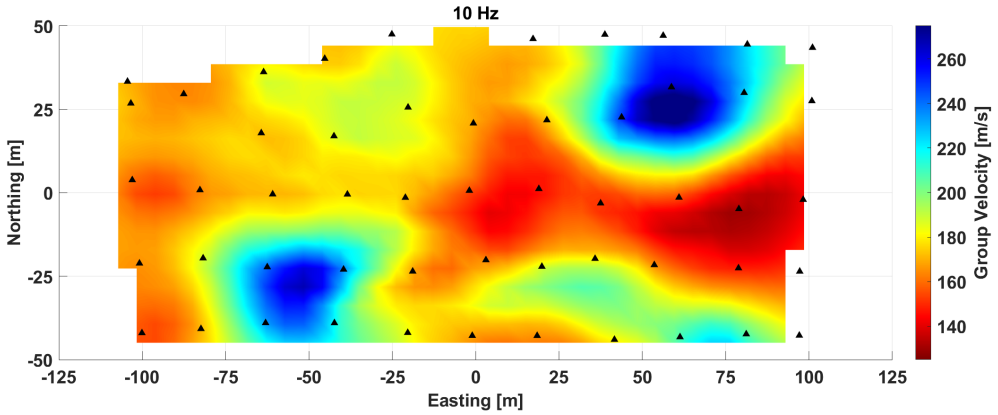

Figure 6.6 2D ambient noise tomography map at 10 Hz

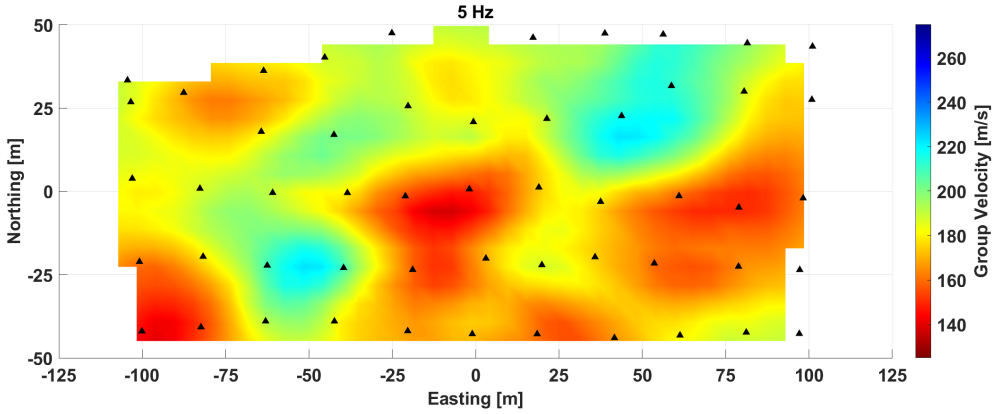

Figure 6.7 2D ambient noise tomography map at 5 Hz.

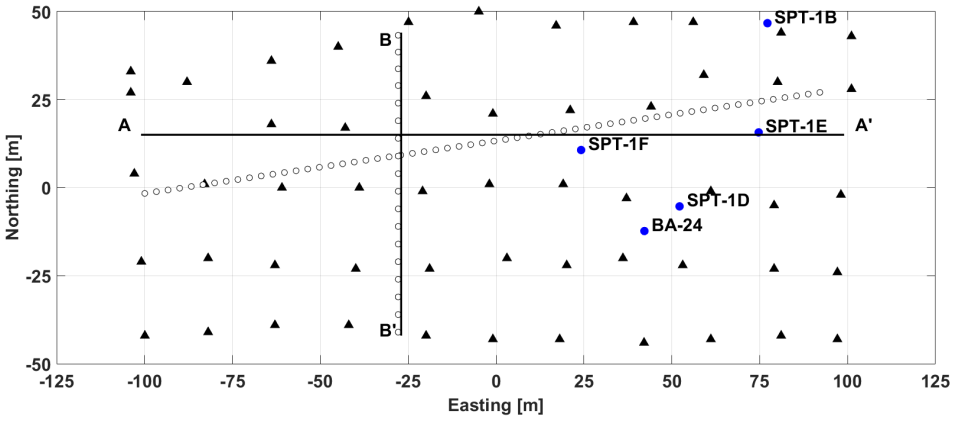

Figure 6.8 Borehole locations with respect to ambient seismic stations (black triangles), electrical resistivity lines (white circles) and cross sections A-A' and B-B'.

Table 6.1 Selected borehole stratigraphy for the GeoPark study area orig-inally compiled by Parker (1992).

Boring	Depth to bedrock (m)
BA-24	4.0
SPT-1B	6.4
SPT-1D	10.7
SPT-1E	9.1
SPT-1F	7.3

and 10 m. This is visible as the transition from red (200 m/s) to green (400 m/s). Another distinct boundary occurs at depths between 10 m and 15 m, visible as the transition from green (400 m/s) to blue (greater than 600 m/s). A depth slice at 10 m shows an estimation of the depth in the model at which the aforementioned boundaries can be represented.

Figure 6.10 recalls the strongest GPR horizon from Figure 6.2 overlaid with a 200 m/s isosurface from the 3D shear wave velocity model in Figure 6.9. Regions with slow (200 m/s) shear wave velocities correspond to locations where the GPR horizon was deepest, namely the large central depression at 25 m E 10 m N and the two smallest depressions at the western and eastern edges of the study area.

The cross section A-A' is shown in Figure 6.11 with boreholes SPT-1E and SPT-1F superimposed on their respective locations in the Easting direction along the section. The depths of the boreholes as shown represent the first contact with the limestone bedrock. The cross section B-B' is shown in Figure 6.12. No borehole data was available for locations near the B-B' cross section. The two distinct shear wave velocity boundaries mentioned earlier can be more easily seen in these two cross sections: A shallow boundary between 5 m and 10 m and a deeper boundary between 10 m and 15 m. Distinct shear wave velocity structures mimicking pipes and cavities are visible throughout both cross sections at depths greater than 5 m, though these features are most clear in the A-A' cross section.

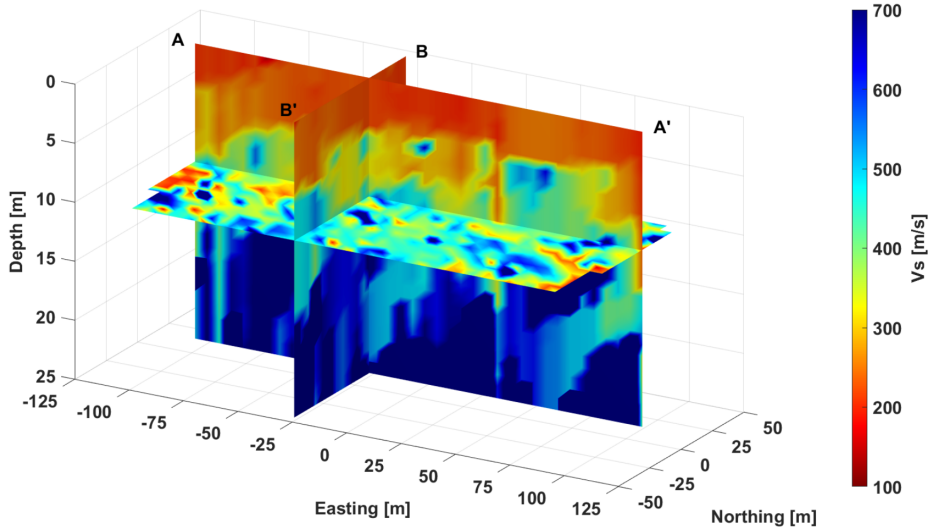

Figure 6.9 Shear wave velocity model with cross sections A-A' and B-B' and a 10 m depth slice.

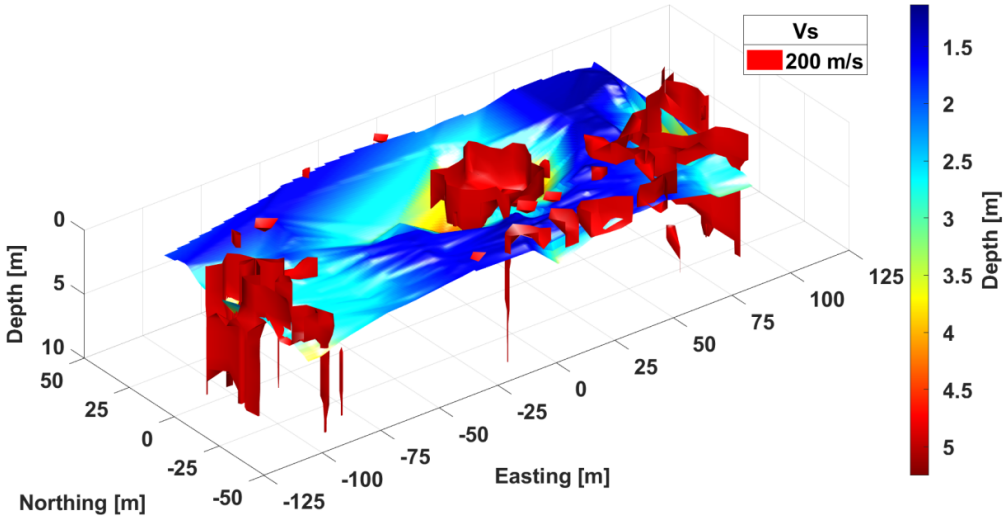

Figure 6.10 GPR horizon from Figure 6.2 overlaid with shear wave velocity model 200 m/s isosurface.

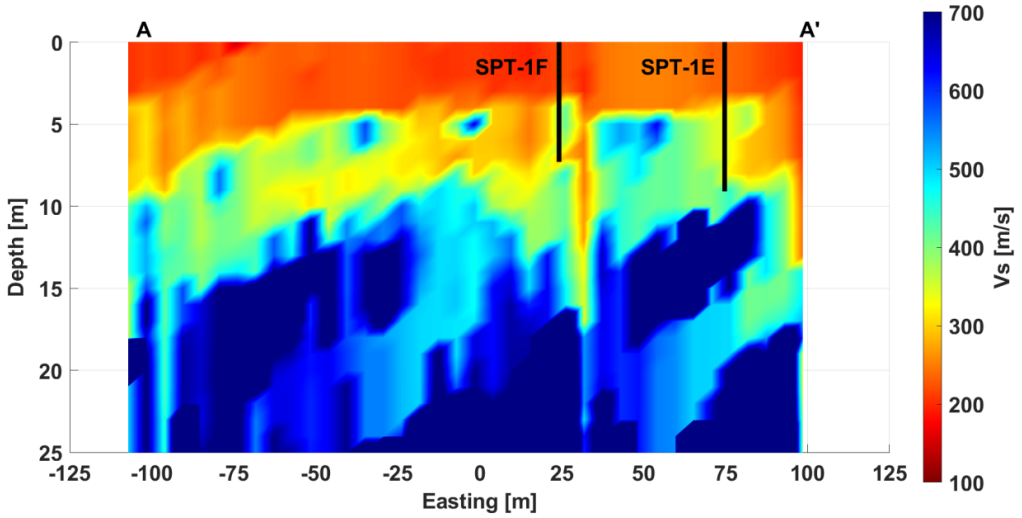

Figure 6.11 Shear wave velocity model along cross section A-A' with superimposed locations of boreholes SPT-1E and SPT-1F and their respective depth to bedrock.

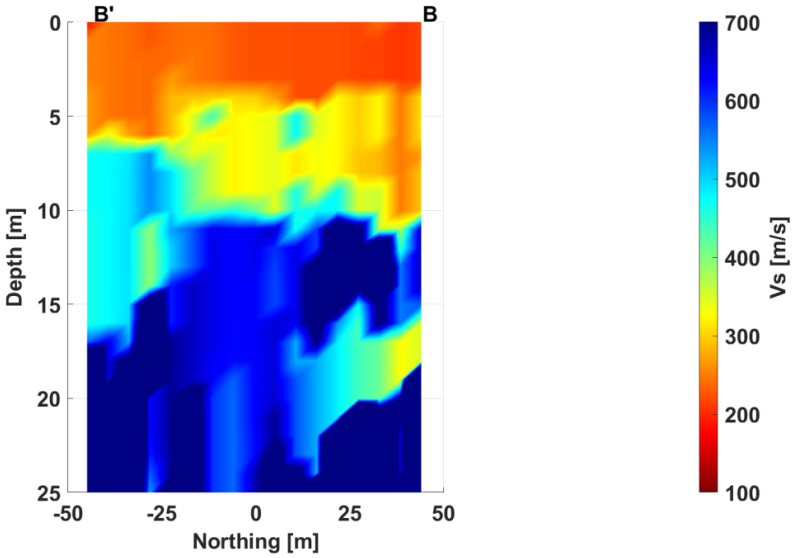

Figure 6.12 Shear wave velocity model along cross section B-B'.

CHAPTER 7:

DISCUSSION

The USF GeoPark is characterized generally by fine sand, silt and clay deposits overlying the Floridian carbonate aquifer. This general lithology is corroborated by ambient noise tomography as well as complementary geophysical surveys and borehole stratigraphy.

7.1 2D Electrical Resistivity Tomography

The highest values (on the order of 10^4 Ohm-m) in the resistivity model shown in Figure 6.1 are reasonable values for dry, unconsolidated sand, and values for soil and carbonate rock are also within the range of the model (McNeill, 1980).

To validate my resistivity results, Diego Domenzain of Colorado School of Mines inverted my data using a separate algorithm (Domenzain *et al.*, 2021) and restricted the resistivity of the model to a maximum amplitude of $5x10^3$ Ohm-m. Those results are shown in Figure 7.1. Despite the limit on the amplitude and using a different regularization strategy, the additional ERT results are very similar to those in Figure 6.1, albeit returning a much smoother model. The gross structure is much the same, but the small-scale features are not consistent across inversions as is to be expected when using different inversion parameters. It is therefore necessary to be cautious with interpreting the small-scale resistivity tomography features at depths

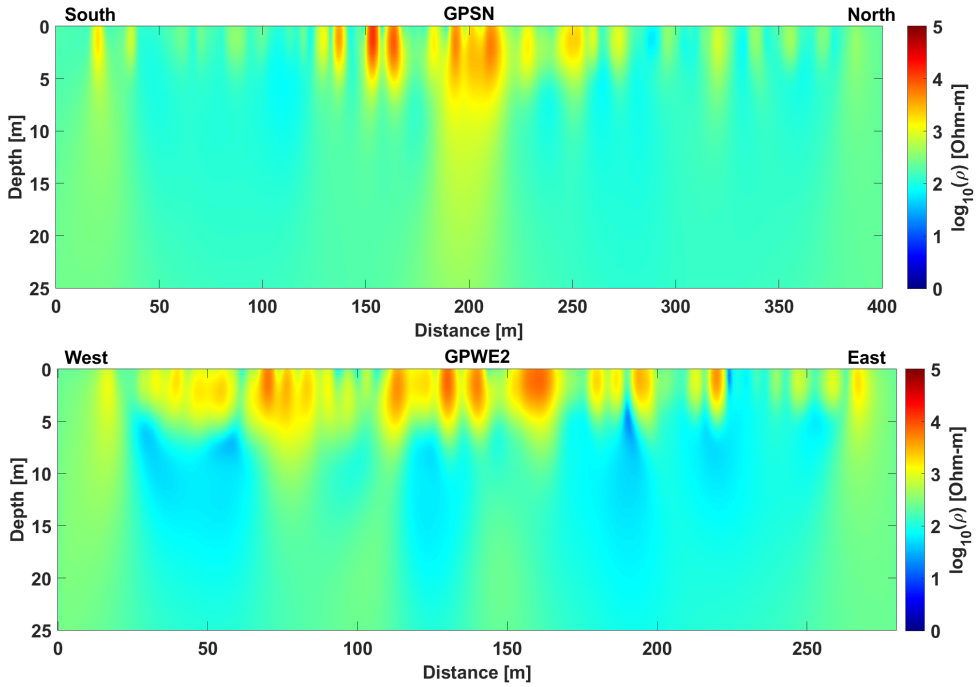

Figure 7.1 Results of the 2D ERT survey of GeoPark using the algorithm of Domenzain *et al.* (2021), south-north line (top) and west-east line (bottom) with 5:1 vertical exaggeration.

below 10 m as that structure cannot be duplicated using the smoother inversion method of Domenzain *et al.* (2021).

Low resistivity and high conductivity zones in the two 2D ERT lines shown in Figure 6.1 could result from saturated or clay-filled cavities or a combination of the two within the limestone basement rock. Low resistivity vertical pipe and point anomalies in the north and east at depths near 10 m are likely conduits and voids forming sinkhole structures in the limestone basement. I associate areas with higher near-surface conductivity (green to blue) with increased soil water content. I interpret the shallow high resistivity zone as the unsaturated zone of the unconsolidated sand and silt overburden. As with the rest of the complementary geophysical data, I am

limited in my combined interpretation to the spatial extent of the passive seismic array (Figures 2.1 and 2.2), shown as vertical black bars in Figure 6.1. In particular, I note the correlation between low resistivity anomalies shown in the eastern half of the west-east ERT line (Distance along the line 130 m to 250 m) from Figure 6.1 and the high group velocity anomaly visible at 60 m E 25 m N in the ambient noise tomography maps, especially at 10 Hz (Figure 6.6).

7.2 Ground Penetrating Radar

Manual picking of the strongest reflector from the common-offset GPR survey (Figure 6.2) reveals depth variability in this horizon of 1 to 5 m. At these depths, this reflector is likely the clay layer overlying the limestone basement. The dominant 5 m depression at 25 m E 10 m N is characteristic of sediments slumping into a void; in this case a suspected 20 m sinkhole formed in the limestone bedrock through chemical weathering processes.

While smaller, the depressions to the west and east of the major suspected sinkhole in Figure 6.2 are also likely candidates for similar void structures underlying the reflective clay layer.

7.3 Ambient Noise Tomography

Figures 6.3 through 6.7 show the ambient noise group velocity tomography results for five frequency bands (5-25 Hz) out of the 24 total frequency maps. As frequency decreases the dispersive nature of surface waves yields the group velocity structure in increasing depth slices.

High group velocity features surrounding a central slow zone are clearly discernible at all frequencies below 28 Hz. This contiguous low velocity zone corresponds to the

suspected sinkhole location at 25 m E 10 m N from the GPR survey (Figure 6.2). As the frequency decreases and depth increases, the slow zones vary in horizontal expression, indicating that there is some variability in the horizontal structure of the shallow sediments.

The high group velocity anomalies are continuous across frequencies, but are also not strictly vertical structures; horizontal variability can be identified in high frequencies corresponding to the shallow subsurface in Figures 6.3 and 6.4. Relative velocities of the faster sediments also vary with depth, most markedly at 5 Hz (Figure 6.7). The high group velocity sediments correspond to the regions where the strongest GPR reflector is shallow.

Findings from the 2D tomography maps are consistent with the complementary geophysical surveys. The slow zone surrounded by faster sediments corresponds to the suspected sinkhole shown by the GPR horizon in Figure 6.2 as well as the areas of high conductivity at 10 m depth at a distance of 150 m along the west-east resistivity section (Figure 6.1).

As detailed in Appendix A, the 2D tomography maps lost resolution above 28 Hz due to the reduced number of raypaths for group velocity constraints at those frequencies.

7.3.1 1D Vs Depth Inversion

As seismic resolution is dependent on the background velocity, the resolution of the final shear wave velocity model varies throughout the combined data cube (Figure 6.9). By Rayleigh's criterion, discussed by Kallweit & Wood (1982), resolving vertical features as small as 1/4 the seismic wavelength is well-established. It is valid to expect similar lateral resolution within the scope and scale of this study. In the

immediate near surface, slow sediment shear wave velocities (around 200 m/s) correspond to a wavelength of approximately 7 m. This depth slice (surface to 10 m) is the primary area of interest for detecting void structures. Given the sampling of seismic wavelengths in this study, it is reasonable to expect feature resolution on the order of 2 to 5 m in the shallow near surface and 30 m approaching the interface of the limestone basement. The vertical pipe feature in Figure 6.11 near borehole SPT-1F has a length scale that is resolved by seismic wavelengths at depths to 10 m.

Figure 7.2 illustrates the velocity disparity between the conduit fill sediment and other higher velocity sediments. The group velocity and shear wave velocity 1D dispersion curves are located on the same respective pixels. The slow sediment curve is associated with the location of the pipe or conduit feature in the center of the array, and the fast sediment curve is associated with a pixel approximately 10 m to the east of the central pipe feature. There is clearly significant variation in the velocity between the two locations, both in the intermediate group velocity tomography and the final shear wave velocity inversion, adding confidence to the interpretation of a conduit feature beneath the central depression in Figure 6.2 and the slow velocity zone in Figure 6.11. The discrepancy between the absolute values for group and shear wave velocity stem from the automated picking of the FTAN group velocity dispersion curves.

Resolution decreases with depth, as velocities at 10 to 15 m (400-600 m/s) correspond to longer wavelengths of up to 120 m. This loss of resolution at depth is still suitable for resolving shear wave velocity contrasts representative of large (30 m and greater) diameter conduits within the consolidated bedrock at depth.

As illustrated by the shear wave velocity fence diagram in Figure 6.9 as well as the

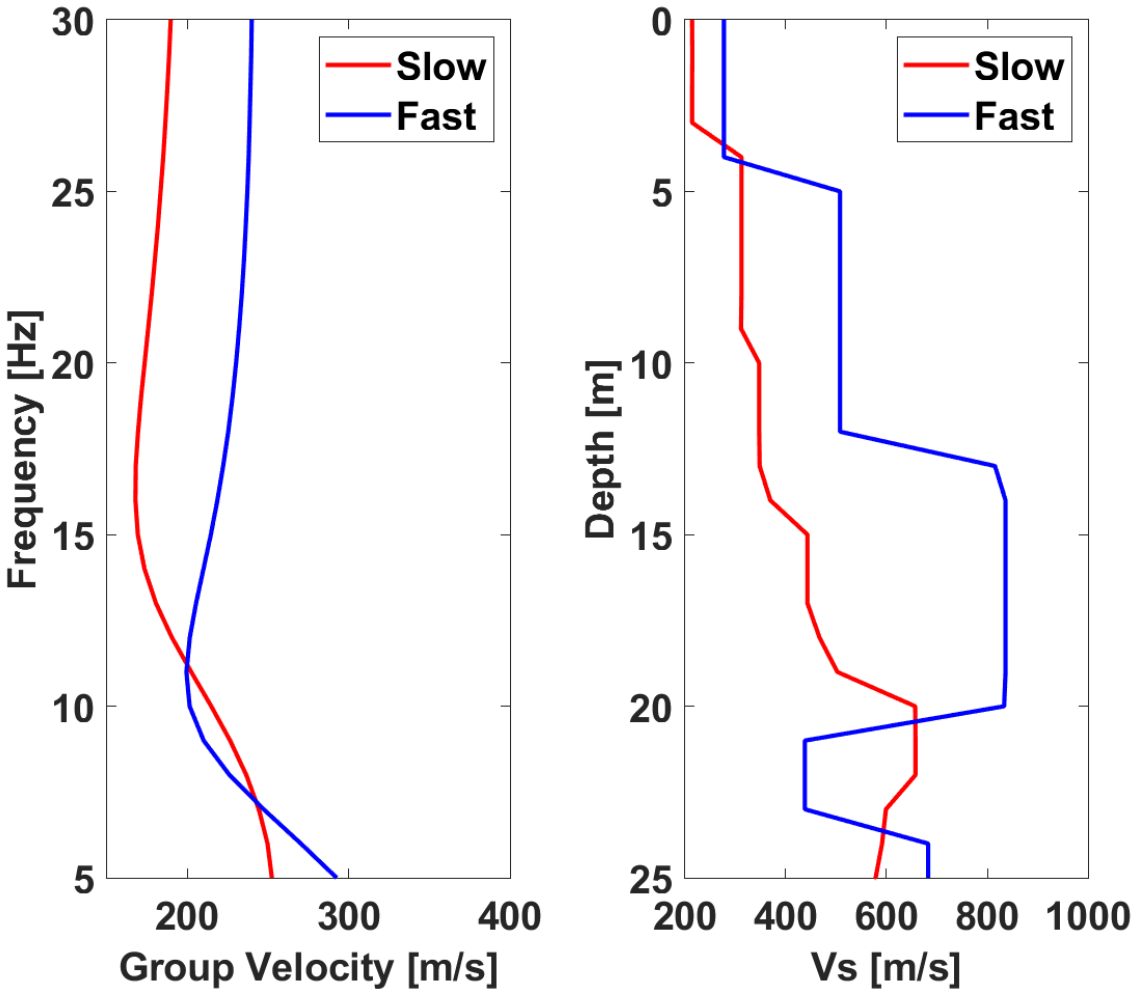

Figure 7.2 Group velocity (left) and shear wave velocity (Vs) (right) dis-persion curves for slow (red) and fast (blue) sediments. The slow sediment curve corresponds to the pipe feature in the center of the array. The fast sediment curve corresponds to a pixel 10 m to the east. The slow and fast curves are in the same geographic location in each respective plot.

cross sections in Figures 6.11 and 6.12, the general fabric of the site shows a southwest-dipping trend, with faster shear wave velocities towards the southwest. Although the two surveys are not in precisely the same location, this trend is consistent with findings from previous surface-wave analysis at the site by Park & Taylor (2010).

Similarly, the groundwater table can be identified from both the resistivity lines (Figure 6.1) and the combined seismic cross sections (Figures 6.11 and 6.12). As resistivity can be related to water content, highly resistive zones in the shallow near surface to depths of around 6 m likely consist of dry unconsolidated sand immediately above the water table. The resistivity tomography used for validation in Figure 7.1 also shows the highly resistive zone and depth to the water table zone as approximately 6 m. The shear wave velocity of the uppermost sediment is in agreement with this interpretation. Slow sediments corresponding to a stiff soil (Building Seismic Safety Council (BSSC), 2003) are expected in unconsolidated sand. The highly resistive zones in the near surface (Figure 6.1) are not strictly horizontal in structure, implying that the surficial sand layer varies in depth.

The aggregate stratigraphy of the site with respect to the shear wave velocity structure is made up of two shear wave velocity boundaries or transition zones visible in Figure 6.11, one occurring at approximately 6 m depth (with velocities increasing from 200 m/s to 400 m/s) and the other at approximately 12 m depth (with velocities increasing again from 400 m/s to greater than 600 m/s). Utilizing the NEHRP site classification criteria in Table 1.1, these sections separated by the two transition zones can be classified as Class D stiff soil in the immediate near surface (Vs between 180-360) to a depth of roughly 6 m, transitioning to Class C very stiff soil and soft rock from 6 m to 12 m, then again to Class B rock after 12 m depth. The results from

the complementary geophysical datasets discussed in sections 7.1 and 7.2 corroborate these findings, particularly that the 200 m/s Class D layer represents unconsolidated sand and conduit fill in the first 5 m to 10 m of depth overlying a clay-rich confining layer.

I constrain the depth to bedrock with borehole stratigraphy compiled by Parker (1992). The recorded depths to the limestone bedrock in Table 6.1 corroborate the conclusion that a clear shear wave velocity boundary exists between 5 m and 10 m in Figure 6.9. As is the nature of subsurface karst expression, this boundary is likely not consistent, varying both in depth and level of weathering present in the limestone. Weathered or fractured limestone with the presence of other sediments near the transition zone or shear wave velocity interface will have a slower velocity than the denser bedrock that remains mostly unaffected by chemical weathering processes. Thus, the Class C soil and soft rock layer in the model stratigraphy with velocities between 400 m/s and 600 m/s at depths between 5 m and 15 m is likely weathered limestone mixed with sand and silt from the overburden. The true bedrock formation consisting of mostly unweathered limestone is therefore the Class B rock as the deepest layer in the model (greater than 15 m depth) with shear wave velocities above 760 m/s.

Near-surface slow shear wave velocity zones (around 200 m/s) in the shear wave velocity model (Figure 6.9) correspond nearly exactly to the three major depressions in the strongest GPR horizon from Figure 6.2: The primary depression being the central suspected sinkhole as well as the smaller depressions in the western and eastern edges of the study area. Overlapping the two datasets leads to the interpretation that these depressions or voids represented by the reflective clay layer have filled in with slow shear wave velocity unconsolidated sand. The west-east electrical resistivity line

(Figure 6.1) approximated by cross section A-A' also shows shallow high resistivity zones approaching 5 m in the same location, around 175 m distance, corresponding to dry, unconsolidated sand overlying the clay layer. Beneath the shallow unconsolidated sediments, the west-east ERT line (at 175 m distance) contains significant high conductivity pipe and void features at depths from 5 m to more than 15 m, implying variability in the karst structure lies deeper than the GPR horizon in Figure 6.2. Cross section A-A' (Figure 6.11) verifies this by way of shear wave velocity anomalies in the area of interest in the shape of pipe and void features from 0 m E to 75 m E at 5 m to 15 m depth. These features contain conduits of slow sediments intruding into the otherwise approximately horizontal stratigraphy as well as isolated high-velocity point anomalies at depths of around 5 m.

7.3.2 Temporal Scale

The temporal monitoring method is not sensitive to fluid flow, but groundwater patterns can otherwise be detected and monitored in the 20-day record with daily time windows. The time scale required for resolving dissolution and collapse features using ambient noise tomography is greater than the data record in this study. However, a fixed array of a similar size with a multi-year noise record would be much more likely to highlight changes to the karst void structures both as incremental dissolution processes and sudden or near-instantaneous conduit collapse events resulting in the formation of a sinkhole.

7.4 Conclusions

By a combined interpretation of geophysical and geotechnical surveys, I have located one likely sinkhole location at 25 m E 10 m N and two smallest suspected expres-

sions of karst structure at the far western and eastern edges of the survey area near -100 m E 0 m N and 85 m E -5 m N, respectively. This analysis is based on anomalies in the shear wave velocity structure in Figure 6.9 combined with electrical resistivity tomography (Figure 6.1) and correlation with variation in the GPR horizon (Figure 6.2) showing areas of preferential gravity-driven groundwater flow in channels. Borehole stratigraphy (Table 6.1) verifies a range corresponding to an average depth to bedrock over the study area.

Taken jointly, these observations merit the conclusion that near-surface areas of high resistivity correspond to slow velocity sediments represented as dry, unconsolidated sand to a maximum depth of 5 m, overlying a highly reflective clay horizon. There exists a shear wave velocity transition between 5 m and 10 m containing weathered and fractured limestone with the inclusion of unconsolidated sediments that have filled gaps left by the weathered bedrock. The velocity increase to 400 m/s is indicative of a change in material. This transition layer is more highly conductive than the dry sand above it, likely containing a higher water content with increased depth. The depth to the unweathered limestone bedrock varies from approximately 10 m to 15 m and corresponds to moderate electrical resistivity and increased shear wave velocities greater than 600 m/s.

It is clear that ambient noise tomography can resolve voids and conduit structure in the karst environment in the form of variation in the shear wave velocity structure. While likely not precise enough for a standalone site characterization method, the ambient noise tomography method and shear wave inversion work well in concert with other more well-established geophysical methods such as electrical resistivity tomography and ground penetrating radar to provide a more accurate representation

of the subsurface in the karst environment.

Ambient noise tomographic methods give a broader picture as to the shear wave velocity structure of the site of interest with greater vertical resolution: This study successfully imaged deeper than previous active-source seismic studies at the GeoPark site (Park & Taylor, 2010) and corroborated results from a suite of complementary geophysical methods.

CHAPTER 8:

FUTURE WORK

Research at the USF GeoPark is ongoing and will continue after this thesis. I have made the data and results available to other project collaborators for future work.

Computation of the Green's function correlations and stacking over the entire recording period of 20 days provides the basis for a single tomographic inversion. However, in order to examine the temporal variation that occurred over the duration of the sensor emplacement I stack the correlation functions on a daily basis. This is an arbitrary length of time and can change depending on the stability of the correlations and desired temporal resolution. I created interferograms of the time series correlation functions for pairs of stations at short, medium, far and very far station offsets (20, 50, 100 and 200 m) for the total 20-day sensor emplacement, shown in Figures 8.1, 8.2, 8.3 and 8.4 respectively.

By stacking on a daily basis, it is clear through the similarity of the correlations that the Green's functions are stable and consistent in a 24-hour period over a variety of station offsets. Slight variations within the 20-day record could be explained by changes in barometric pressure or periodic cultural activity, though would be difficult to make a conclusive, qualitative assessment over such a small recording window using hourly weather observations. However, there is a clear difference in the noise correlations during the weekends, which occurred on March 23rd and 24th, as well

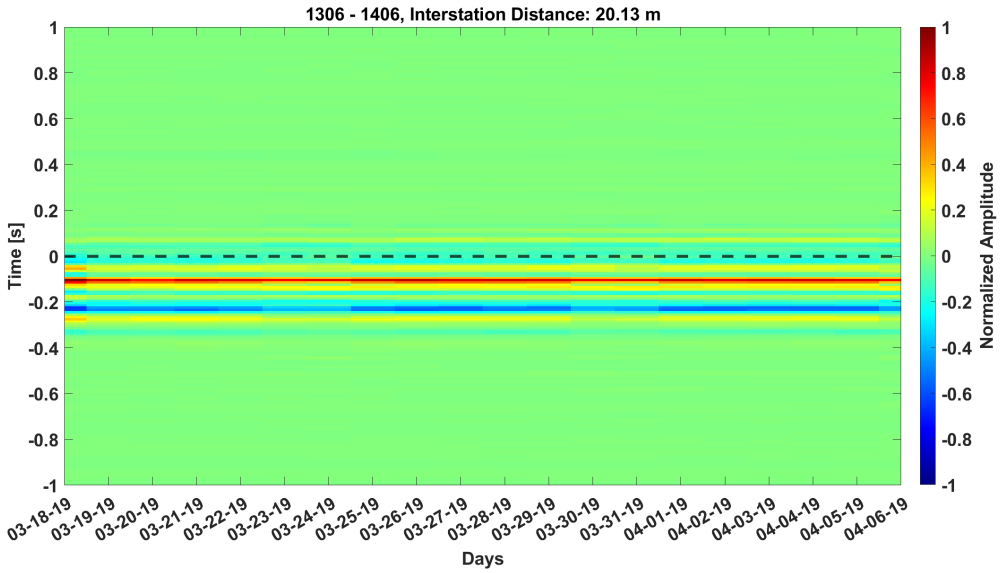

Figure 8.1 Interferogram for a single station combination (20 m offset) with daily stacking over the total 20-day sensor emplacement.

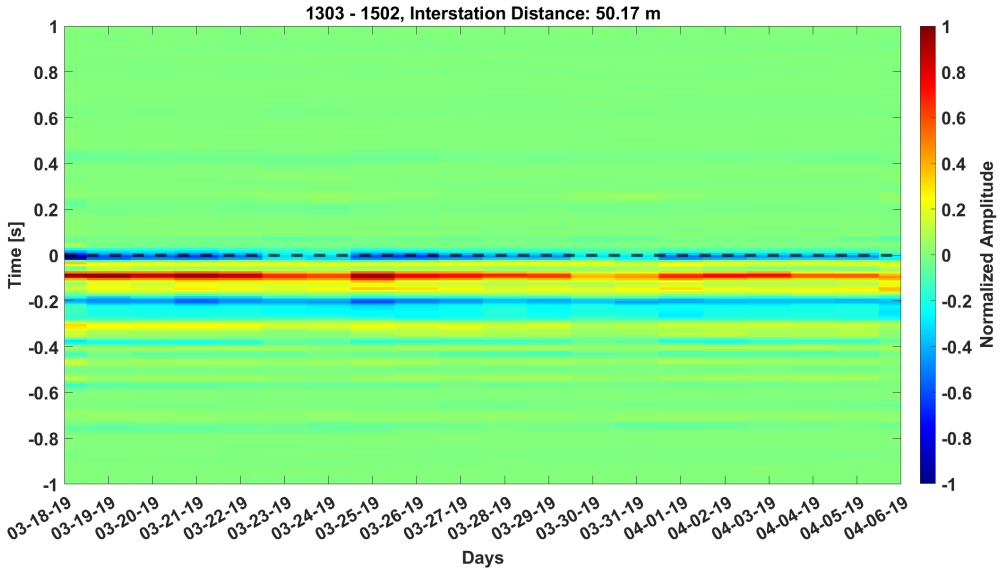

Figure 8.2 Interferogram for a single station combination (50 m offset) with daily stacking over the total 20-day sensor emplacement.

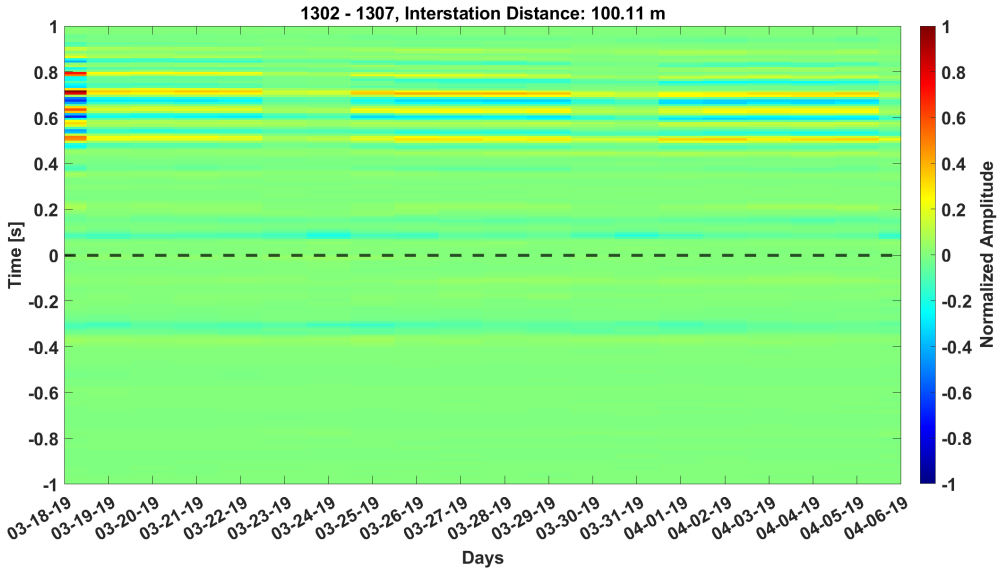

Figure 8.3 Interferogram for a single station combination (100 m offset) with daily stacking over the total 20-day sensor emplacement.

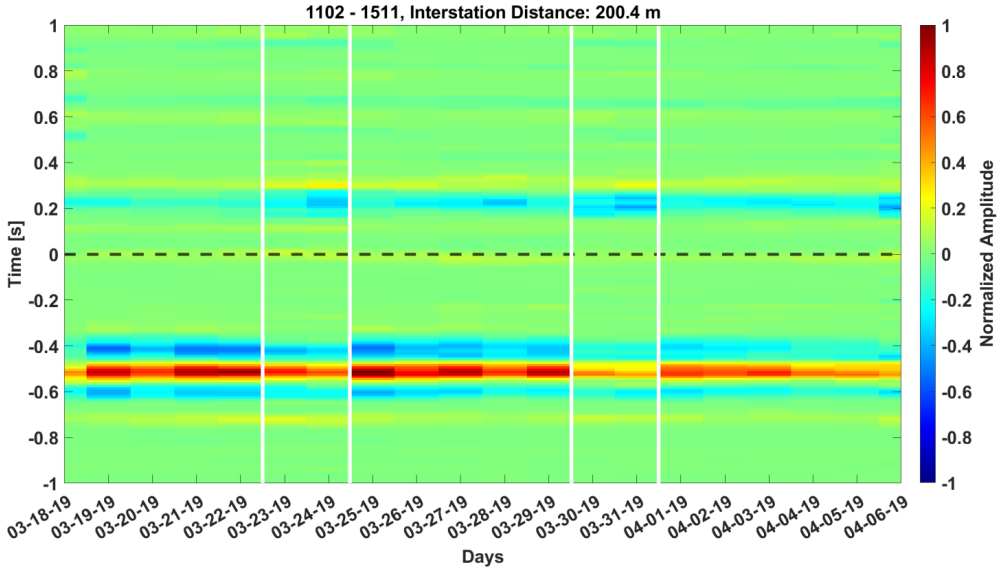

Figure 8.4 Interferogram for a single station combination (200 m offset) with daily stacking over the total 20-day sensor emplacement. White vertical bars highlight weekends.

as March 30th and 31st. These dates are bounded in Figure 8.4. This change in the correlation functions is probably due to variation in cultural noise, particularly a decrease in the amount of vehicle traffic on the USF campus during the weekend.

The decrease in noise amplitude over the weekends has the effect of making the cross-correlation functions on those days more symmetrical, as a lower noise amplitude in the immediate vicinity is not present to wash out or obstruct sources from further away. Based on the interferogram, the weekend record consists of road noise from a greater distance (perhaps highways adjacent to and outside the USF campus) where the sources are more symmetrical, as they arrive from a wider range of azimuths.

It is clear that the method of temporal monitoring using ambient noise tomography is valid but that the recording period should be extended to include both larger discrete events that may occur on a longer timescale. No clear discrete events such as conduit collapse or sinkhole formation are recorded in these 20-day interferograms.

The primary direction for future work in ambient noise tomography at this site involves extending the methods for temporal monitoring in site characterization. This would require a long-term sensor array emplacement of months to years. Instead of generating a single 3D shear wave velocity model to describe the structure, a model could be developed at periodic intervals such as every month or annually in order to monitor larger changes to the subsurface velocity structure that would occur from conduit collapse and sinkhole formation.

Additionally, the existing record could be analyzed in a similar manner, albeit on a shorter timescale. This can be accomplished by performing crosscorrelations on time windows shorter than the full 20-day period to analyze small spatio-temporal changes in the subsurface over the entire data record. For this noise record, the time windows

can be anywhere from one hour to one week in length, depending on application and requirements. This approach could also include shrinking the inversion cell size to attempt an improvement on spatial resolution. No conduit collapse or structure changes would likely be resolved, but it is possible to monitor changes in soil water content and mechanical properties of the study area.

Future work could also examine the radial component to determine particle motion, or use beamforming techniques to determine the directionality of the energy source to assess how well the source surrounds the study area.

8.1 Recommendations

8.1.1 Site characterization in karst environment

Any geophysical site characterization in karst should begin with an initial GPR survey to establish zones of interest. GPR is clearly an excellent tool for identifying depressions that are diagnostic for void structures in carbonate aquifers. Once the focus has been narrowed, performing ambient noise tomography with a short-duration emplacement of a passive seismic array is a cheap, robust method for extracting the 3D shear wave velocity structure in a karst environment. As found in this research, site-scale ambient seismic tomography can locate and characterize void structures and other shear wave velocity anomalies in karst.

Lastly, it would be desirable to perform direct sampling in the suspected sinkhole location to characterize the material properties of the sediment within and beneath the collapsed conduit. This would also serve to validate the shear wave velocity model.

Since ground-penetrating radar appears to be the most promising tool to delineate reflective horizons at the site scale, a joint inversion could be employed using GPR to

constrain depth, improving the accuracy of the resulting shear wave velocity model.

8.1.2 Spatio-temporal monitoring in karst environment

Similarly to a tomographic site characterization application, spatio-temporal monitoring in karst environments should begin with a GPR survey to establish zones of interest. If passive seismic is to be used, a long-duration emplacement of a passive array is a requirement. The noise record and crosscorrelation functions can be used to create tomographic inversions on a periodic basis. The Green's functions from this method are stable enough to perform daily tomographic inversions, but structural changes will only be apparent on a much longer temporal scale. In addition to these long-duration changes to the karst structure, potentially including conduit collapse and sinkhole formation, such an application has the potential to expose seasonal trends in groundwater level and aquifer recharge.

REFERENCES

Anderson, Neil, Croxton, Neil, Hoover, Rick, & Sirles, Phil. 2008. Geophysical Methods Commonly Employed for Geotechnical Site Characterization. *Transportation Research Circular, Transportation Research Board of the National Academies*, **E-C130**(October).

Bansah, Kenneth J., & Anderson, Neil L. 2018. Mapping subsurface in karst terrain using 2-D electrical resistivity tomography. *In: Proceedings of the Symposium on the Application of Geophyics to Engineering and Environmental Problems, SAGEEP*, vol. 2018-March.

Barde-Cabusson, Stéphanie, Finizola, Anthony, & Grobbe, Niels. 2020. a Practical Approach for Self-Potential Data Acquisition, Processing, and Visualization. *Interpretation*, **9**(1), 1–67.

Barmin, M. P., Ritzwoller, M. H., & Levshin, A. L. 2001. A fast and reliable method for surface wave tomography. *Pure and Applied Geophysics*, **158**(8), 1351–1375.

Bédard, Mylène. 2008. Optimal acceptance rates for Metropolis algorithms: Moving beyond 0.234. *Stochastic Processes and their Applications*.

Bensen, G. D., Ritzwoller, M. H., & Shapiro, N. M. 2008. Broadband ambient noise

surface wave tomography across the United States. *Journal of Geophysical Research: Solid Earth*, **113**(5), 1–21.

Boston, P. J., Spilde, M. N., Northup, D. E., Melim, L. A., Soroka, D. S., Kleina, L. G., Lavoie, K. H., Hose, L. D., Mallory, L. M., Dahm, C. N., Crossey, L. J., & Schelble, R. T. 2001. Cave biosignature suites: Microbes, minerals, and Mars. *Astrobiology*.

Boston, Penelope J. 2010. Location, Location, Location!. Lava Caves on Mars for Habitat, Resources, and the Search for Life. *J. of Cosmology*.

Boston, Penelope J., Ivanov, Mikhail V., & P. McKay, Christopher. 1992. On the possibility of chemosynthetic ecosystems in subsurface habitats on Mars. *Icarus*.

Brenguier, Florent, Shapiro, Nikolai M., Campillo, Michel, Nercessian, Alexandre, & Ferrazzini, Valérie. 2007. 3-D surface wave tomography of the Piton de la Fournaise volcano using seismic noise correlations. *Geophysical Research Letters*, **34**(2), 2–6.

Building Seismic Safety Council (BSSC). 2003. NEHRP Recommended Provisions for Seismic Regulations for New Buildings and Other Structures, Part 1-Provisions. *Part 1*, 338.

Bumpus, Peter B., & Kruse, Sarah E. 2014. Self-potential monitoring for hydrologic investigations in urban covered-karst terrain. *Geophysics*, **79**(6), B231–B242.

Campillo, Michel, & Paul, Anne. 2003. Long range correlations in the diffuse seismic coda. *Science*, **299**(5606), 547–549.

Claerbout, Jon F. 1968. Synthesis of a layed medium from its acoustic transmission response. *GEOPHYSICS*, **33**(2), 229–392.

Curtis, Andrew, Gerstoft, Peter, Sato, Haruo, Snieder, Roel, & Wapenaar, Kees. 2006. Seismic interferometry - Turning noise into signal. *Leading Edge (Tulsa, OK)*, **25**(9), 1082–1092.

Dobecki, Thomas L., & Upchurch, Sam B. 2006. Geophysical applications to detect sinkholes and ground subsidence. *Leading Edge (Tulsa, OK)*, **25**(3), 336–341.

Domenzain, Diego, Bradford, John, & Mead, Jodi. 2021. Efficient inversion of 2.5D electrical resistivity data using the discrete adjoint method. *GEOPHYSICS*.

Draganov, Deyan, & Ruigrok, Elmer. 2014. Encyclopedia of Earthquake Engineering. *Encyclopedia of Earthquake Engineering*, 1–13.

Dreiling, Jennifer, & Tilmann, F. 2019. *BayHunter – McMC transdimensional Bayesian inversion of receiver functions and surface wave dispersion.*

Dreiling, Jennifer, Tilmann, Frederik, Yuan, Xiaohui, Haberland, Christian, & Seneviratne, S. W.Mahinda. 2020. Crustal Structure of Sri Lanka Derived From Joint Inversion of Surface Wave Dispersion and Receiver Functions Using a Bayesian Approach. *Journal of Geophysical Research: Solid Earth*, **125**(5), 1–15.

Grobbe, N, & Barde-Cabusson, S. 2019. Self-Potential Studies in Volcanic Environments: A Cheap and Efficient Method for Multiscale Fluid-Flow Investigations. *International Journal of Geophysics*, **2019**, 2985824.

Guerin, Gauthier, Rivet, Diane, Deschamps, Anne, Larroque, Christophe, Mordret, Aurélien, Dessa, Jean Xavier, & Martin, Xavier. 2019. High resolution ambient noise tomography of the Southwestern Alps and the Ligurian margin. *Geophysical Journal International*, **220**(2), 806–820.

Halliday, David, Curtis, Andrew, & Kragh, Ed. 2008. Seismic surface waves in a suburban environment: Active and passive interferometric methods. *Leading Edge (Tulsa, OK)*, **27**(2), 210–218.

Kallweit, R. S., & Wood, L. C. 1982. The limits of resolution of zero-phase wavelets. *Geophysics*.

Kaufmann, Georg. 2009. Modelling karst geomorphology on different time scales. *Geomorphology*, **106**(1-2), 62–77.

Kaufmann, Georg. 2014. Geophysical mapping of solution and collapse sinkholes. *Journal of Applied Geophysics*, **111**, 271–288.

Kiflu, H., Kruse, S., Loke, M. H., Wilkinson, P. B., & Harro, D. 2016. Improving resistivity survey resolution at sites with limited spatial extent using buried electrode arrays. *Journal of Applied Geophysics*, **135**, 338–355.

Kimman, W. P., & Trampert, J. 2010. Approximations in seismic interferometry and their effects on surface waves. *Geophysical Journal International*, **182**(1), 461–476.

Kruse, S., Grasmueck, M., Weiss, M., & Viggiano, D. 2006. Sinkhole structure imaging in covered Karst terrain. *Geophysical Research Letters*, **33**(16), 1–6.

Lecocq, Thomas, Caudron, Corentin, & Brenguier, Florent. 2014. Msnoise, a python package for monitoring seismic velocity changes using ambient seismic noise. *Seismological Research Letters*, **85**(3), 715–726.

Levshin, A., Ratnikova, L., & Berger, J. 1992. Peculiarities of surface-wave propagation across central Eurasia. *Bulletin - Seismological Society of America*, **82**(6), 2464–2493.

Levshin, A L, Pisarenco, V F, & Pogrebinsky, G A. 1972. On a frequency-time analysis of oscillations. *Annales Geophysicae*, **28**(July), 211–218.

Lin, Fan Chi, Ritzwoller, Michael H., Townend, John, Bannister, Stephen, & Savage, Martha K. 2007. Ambient noise Rayleigh wave tomography of New Zealand. *Geophysical Journal International*, **170**(2), 649–666.

Lin, Fan Chi, Moschetti, Morgan P., & Ritzwoller, Michael H. 2008. Surface wave tomography of the western United States from ambient seismic noise: Rayleigh and Love wave phase velocity maps. *Geophysical Journal International*, **173**(1), 281–298.

Maupin, Molly A., & Barber, Nancy L. 2000. Estimated withdrawals from principal aquifers in the United States, 2000. *US Geological Survey Circular*.

McNeill, J.D. 1980. *Electrical conductivity of soils and rocks*.

Miller, James A. 1990. Ground Water Atlas of the United States: Segment 6, Alabama, Florida, Georgia, South Carolina. *Hydrologic Atlas*.

Mordret, A., Landés, M., Shapiro, N. M., Singh, S. C., Roux, P., & Barkved, O. I. 2013. Near-surface study at the valhall oil field from ambient noise surface wave tomography. *Geophysical Journal International*, **193**(3), 1627–1643.

Moschetti, M. P., Ritzwoller, M. H., & Shapiro, N. M. 2007. Surface wave tomography of the western United States from ambient seismic noise: Rayleigh wave group velocity maps. *Geochemistry, Geophysics, Geosystems*, **8**(8), 1–10.

Nishida, Kiwamu, Montagner, Jean Paul, & Kawakatsu, Hitoshi. 2009. Global surface wave tomography using seismic hum. *Science*, **326**(5949), 112.

Park, Choon B., & Taylor, Chris. 2010. 3D MASW Characterization of sinkhole: A pilot study at USF geology park, Tampa, FL. *Proceedings of the Symposium on the Application of Geophyics to Engineering and Environmental Problems, SAGEEP*, **1**, 498–507.

Parker, John W. 1992. *Surficial aquifer hydrogeology in a covered-karst terrane*. M.S., University of South Florida.

Sabra, Karim G., Gerstoft, Peter, Roux, Philippe, Kuperman, W. A., & Fehler, Michael C. 2005. Surface wave tomography from microseisms in Southern California. *Geophysical Research Letters*, **32**(14), 1–4.

Schimmel, Martin, & Paulssen, Hanneke. 1997. Noise reduction and detection of weak, coherent signals through phase-weighted stacks. *Geophysical Journal International*, **130**(2), 497–505.

Seats, Kevin J., Lawrence, Jesse F., & Prieto, German A. 2012. Improved ambient noise correlation functions using Welch's method. *Geophysical Journal International*, **188**(2), 513–523.

Shapiro, N. M., & Campillo, M. 2004. Emergence of broadband Rayleigh waves from correlations of the ambient seismic noise. *Geophysical Research Letters*, **31**(7), 8–11.

Shapiro, Nikolai M., Campillo, Michel, Stehly, Laurent, & Ritzwoller, Michael H. 2005. High-resolution surface-wave tomography from ambient seismic noise. *Science*, **307**(5715), 1615–1618.

Sloan, Steven D., Peterie, Shelby L., Miller, Richard D., Ivanov, Julian, Schwenk, J. Tyler, & McKenna, Jason R. 2015. Detecting clandestine tunnels using near-surface seismic techniques. *Geophysics*, **80**(5), EN127–EN135.

Stehly, Lolo, Fry, B., Campillo, M., Shapiro, N. M., Guilbert, J., Boschi, L., & Giardini, D. 2009. Tomography of the Alpine region from observations of seismic ambient noise. *Geophysical Journal International*, **178**(1), 338–350.

Tihansky, Ann B. 1999. Sinkholes, west-central Florida. *Land subsidence in the United States: US geological survey circular*, **1182**, 121–140.

Ungureanu, Constantin, Priceputu, Adrian, Bugea, Adrian Liviu, & Chirică, Anton. 2017. Use of electric resistivity tomography (ERT) for detecting underground voids on highly anthropized urban construction sites. *Procedia Engineering*, **209**, 202–209.

Wapenaar, Kees. 2004. Retrieving the elastodynamic Green's function of an arbitrary inhomogeneous medium by cross correlation. *Physical Review Letters*, **93**(25), 1–4.

Wapenaar, Kees, & Fokkema, Jacob. 2006. Green's function representations for seismic interferometry. *GEOPHYSICS*, **71**(4).

White, W., Herman, E., Rutigliano, M., Herman, J., Vesper, D., & Engel, S. 2016. Karst Groundwater Contamination and Public Health. *Pages 17–25 of: Karst Groundwater Contamination and Public Health.*

Williams, K. E., McKay, Christopher P., Toon, O. B., & Head, James W. 2010. Do ice caves exist on Mars? *Icarus.*

Yang, Yingjie, Ritzwoller, Michael H., Levshin, Anatoli L., & Shapiro, Nikolai M. 2007. Ambient noise Rayleigh wave tomography across Europe. *Geophysical Journal International*, **168**(1), 259–274.

Youssef, Ahmed M., El-Kaliouby, Hesham, & Zabramawi, Yasser A. 2012. Sinkhole detection using electrical resistivity tomography in Saudi Arabia. *Journal of Geophysics and Engineering*, **9**(6), 655–663.

Zheng, Sihua, Sun, Xinlei, Song, Xiaodong, Yang, Yingjie, & Ritzwoller, Michael H. 2008. Surface wave tomography of China from ambient seismic noise correlation. *Geochemistry, Geophysics, Geosystems*, **9**(5), 1–8.

Zhou, Wanfang, Beck, Barry F., & Adams, Angela L. 2002. Effective electrode array in mapping karst hazards in electrical resistivity tomography. *Environmental Geology.*

APPENDIX A:

2D TOMOGRAPHY MAPS OF GEOPARK STUDY AREA

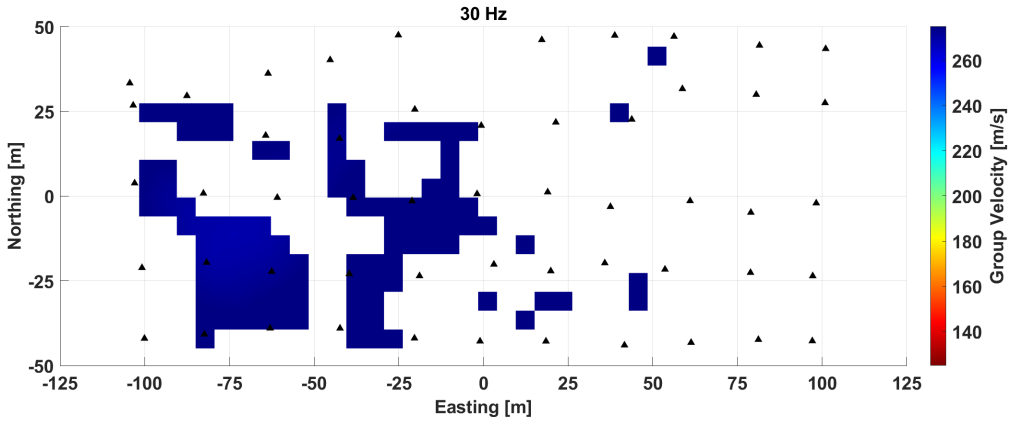

Figure A.1 30 Hz, data removed from the 1D Vs inversion.

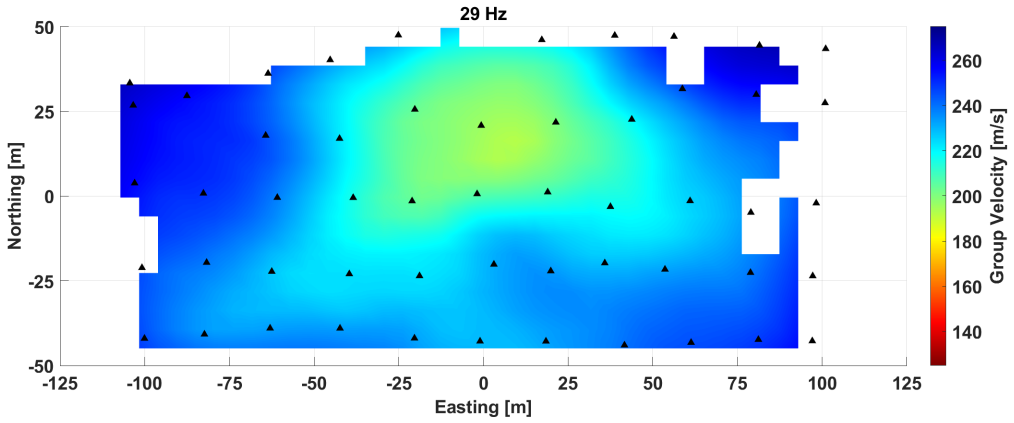

Figure A.2 29 Hz, data removed from the 1D Vs inversion.

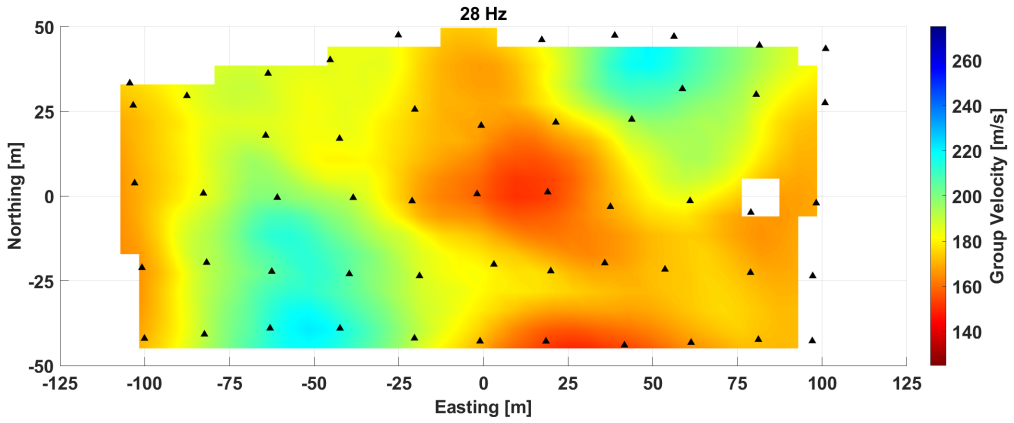

Figure A.3 28 Hz

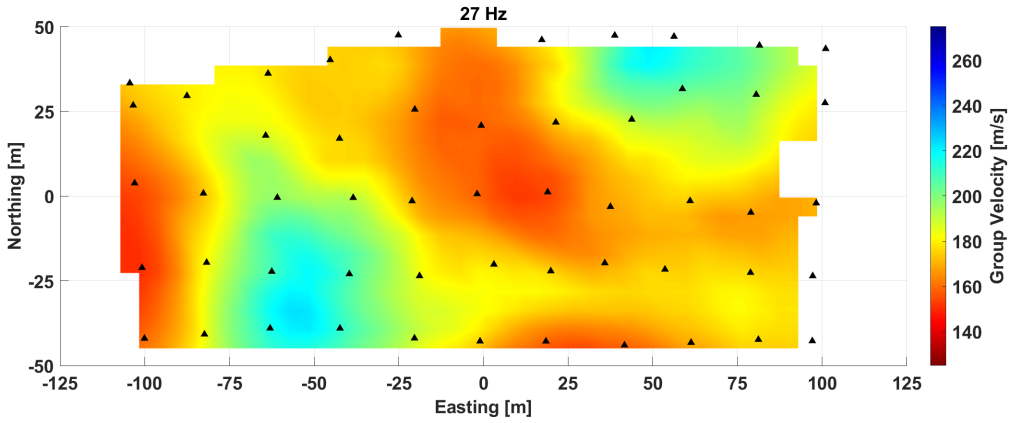

Figure A.4 27 Hz

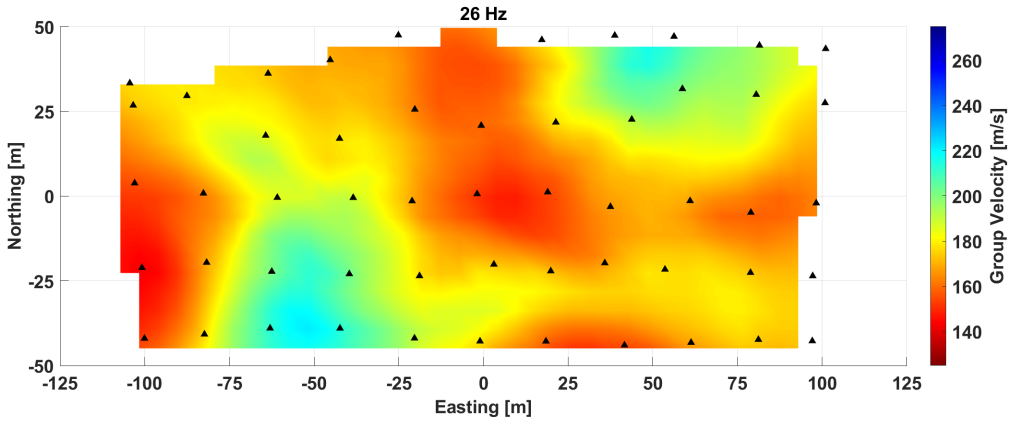

Figure A.5 26 Hz

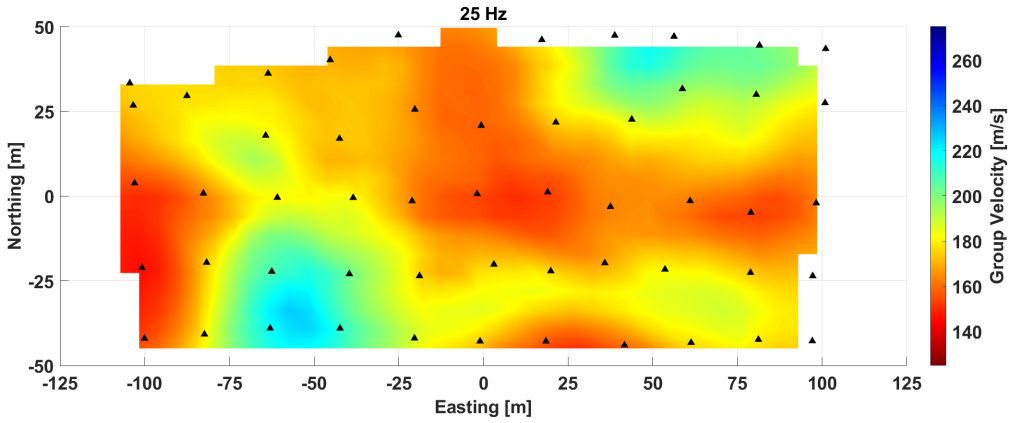

Figure A.6 25 Hz

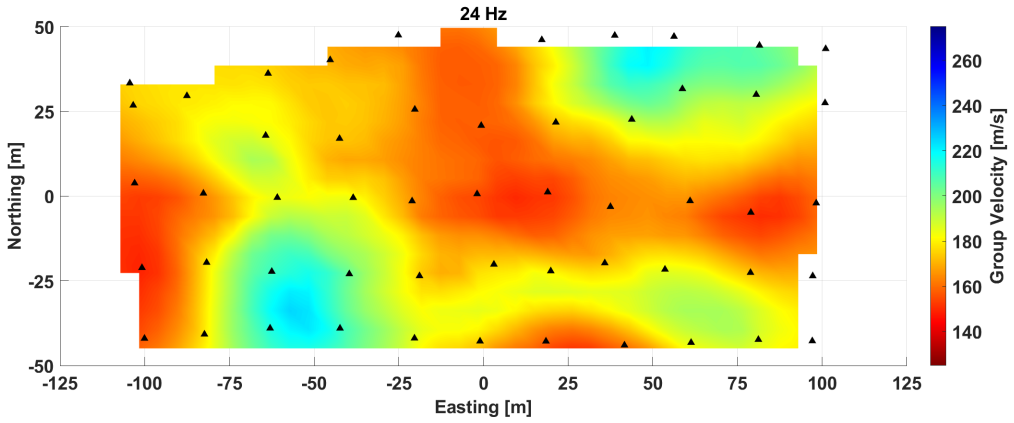

Figure A.7 24 Hz

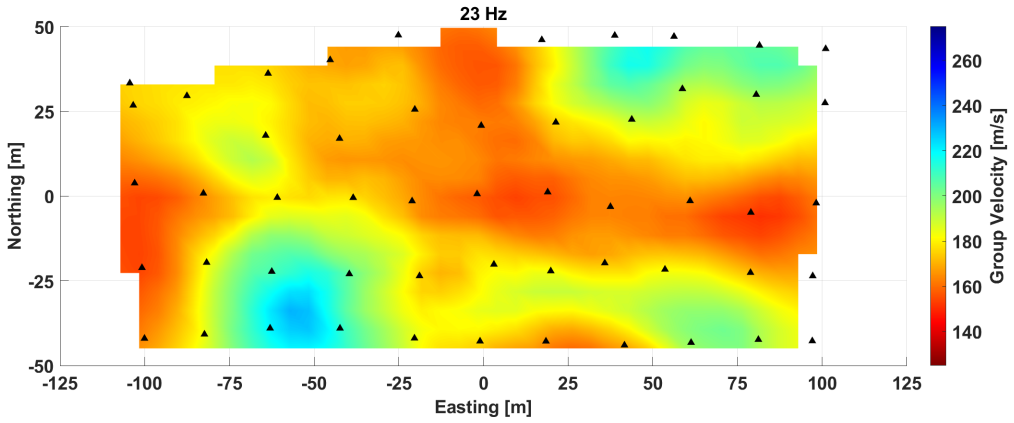

Figure A.8 23 Hz

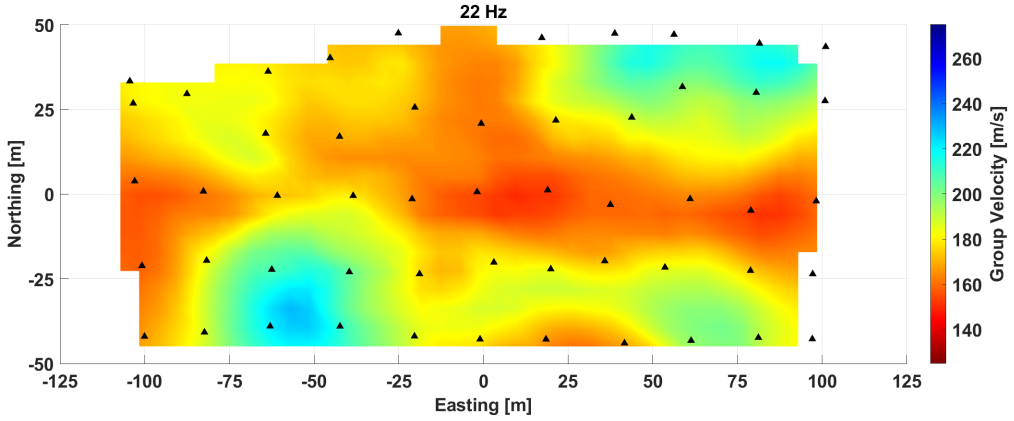

Figure A.9 22 Hz

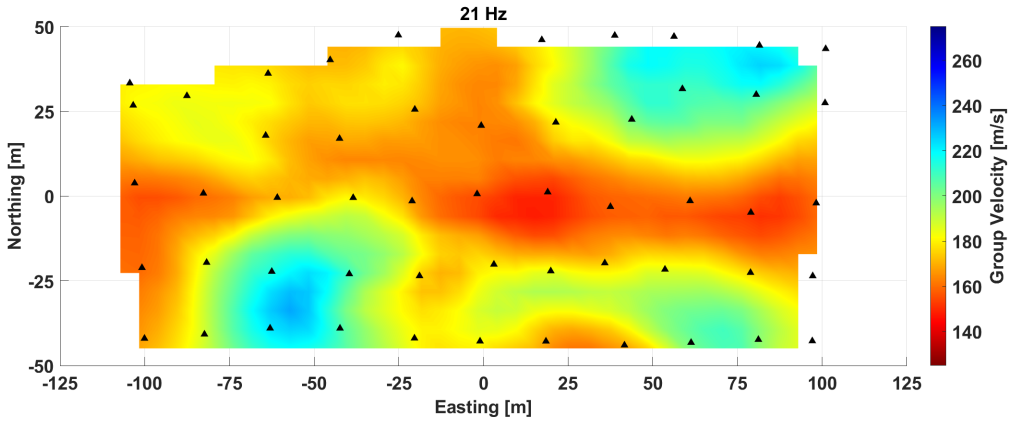

Figure A.10 21 Hz

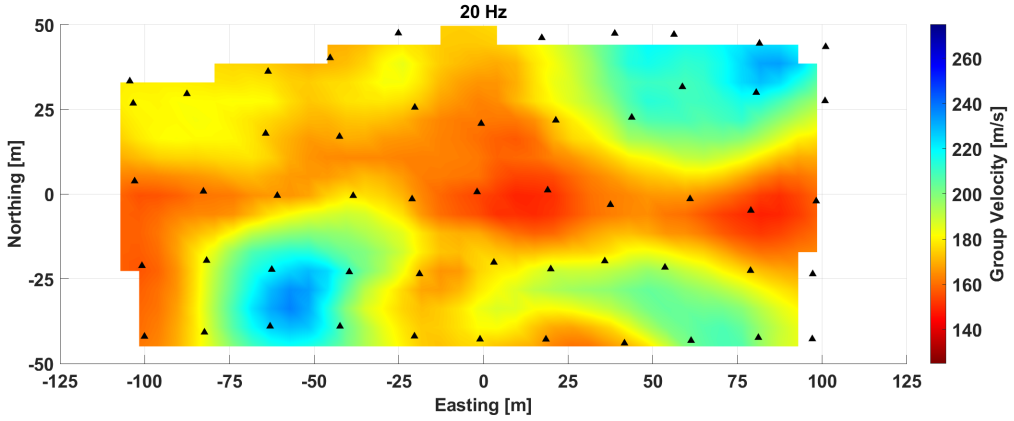

Figure A.11 20 Hz

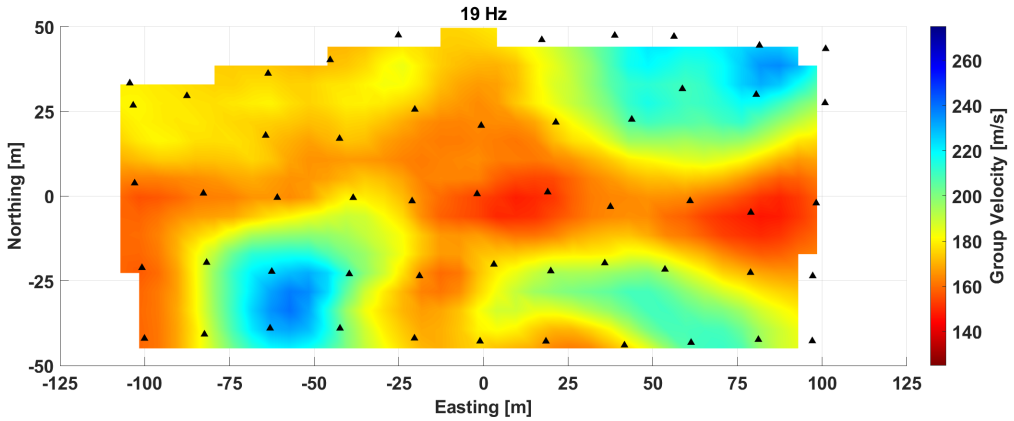

Figure A.12 19 Hz

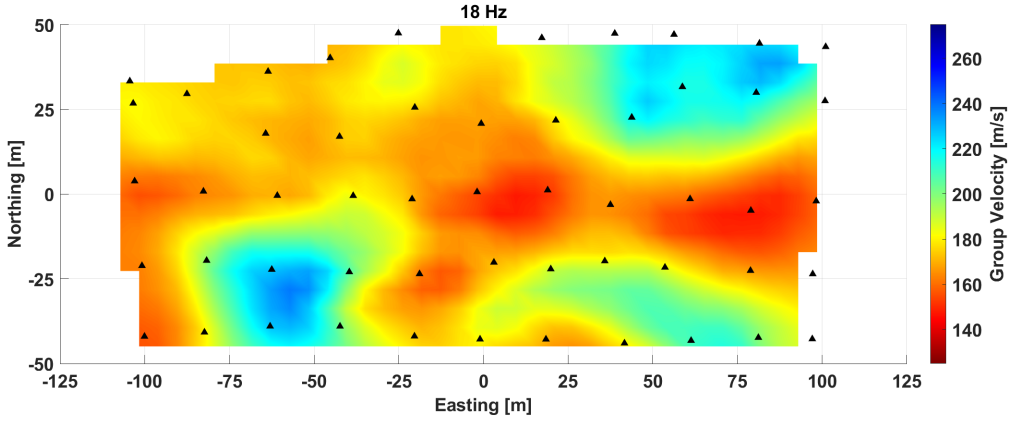

Figure A.13 18 Hz

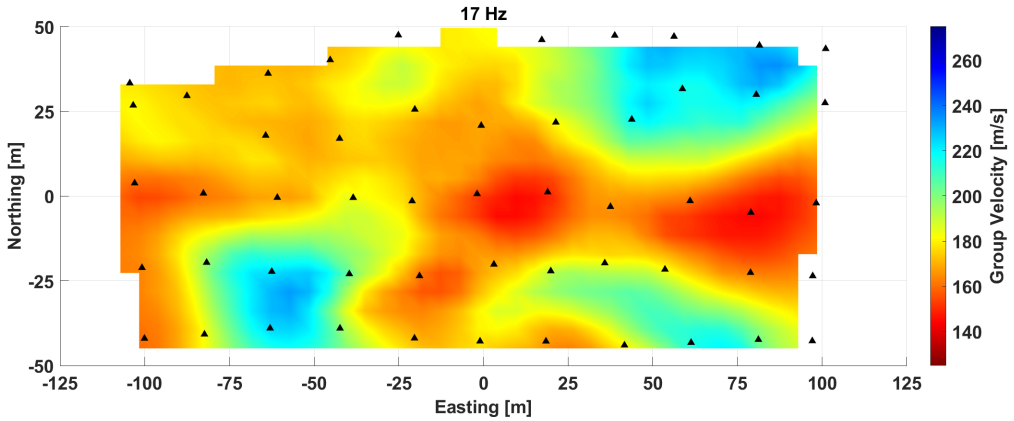

Figure A.14 17 Hz

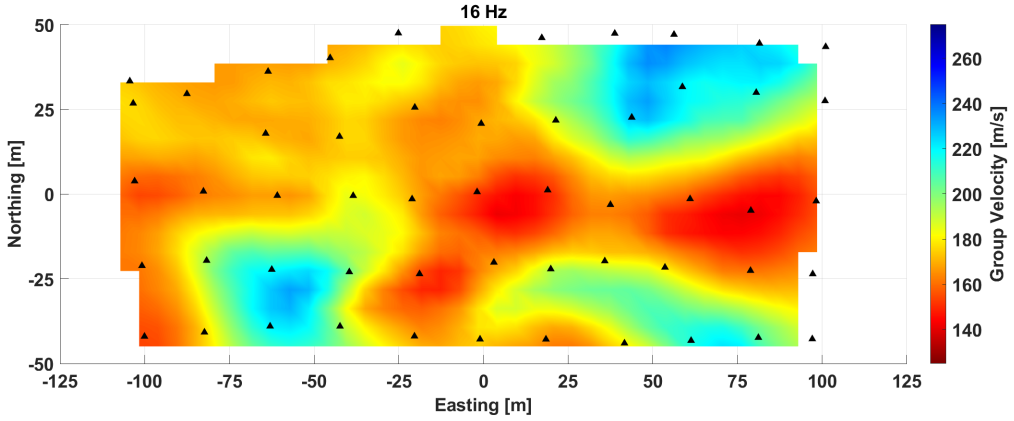

Figure A.15 16 Hz

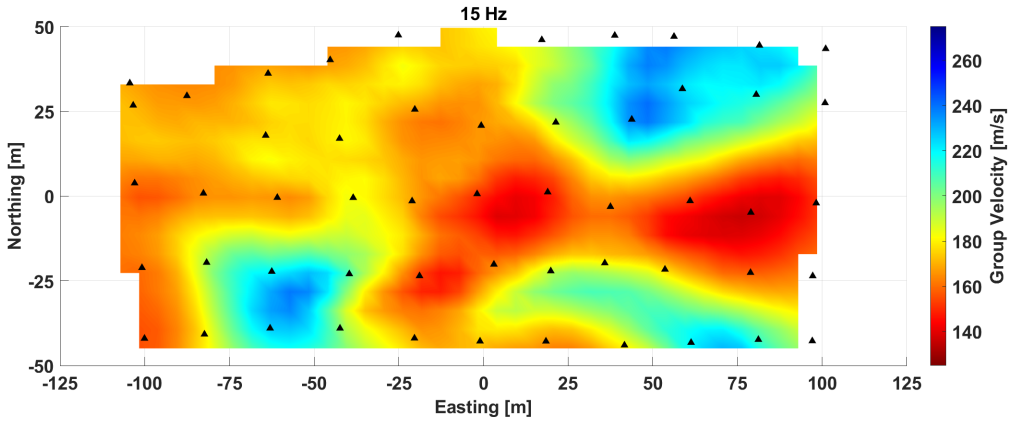

Figure A.16 15 Hz

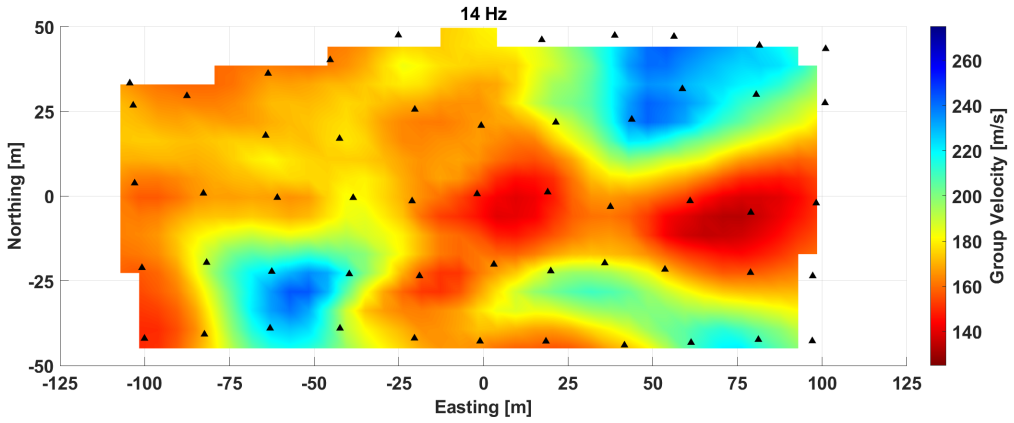

Figure A.17 14 Hz

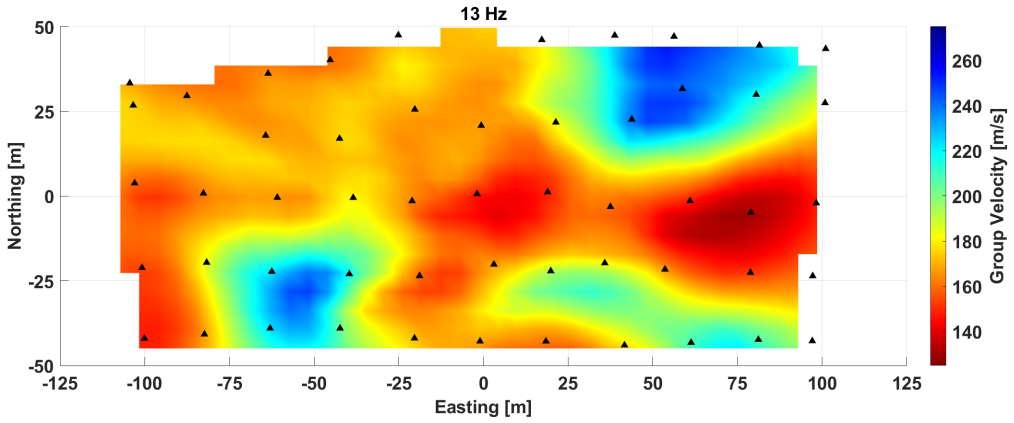

Figure A.18 13 Hz

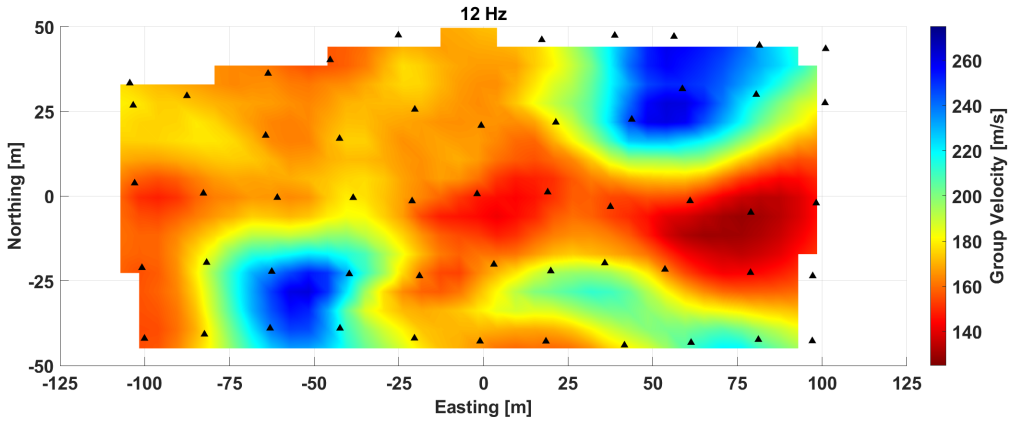

Figure A.19 12 Hz

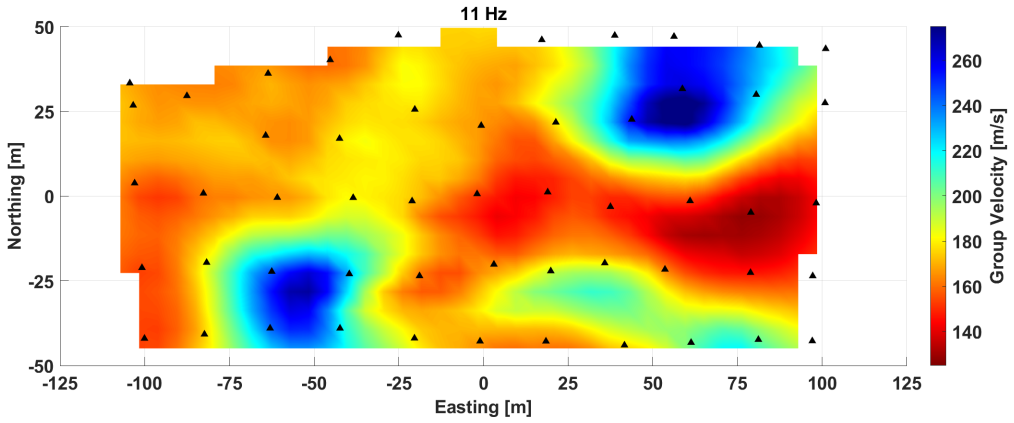

Figure A.20 11 Hz

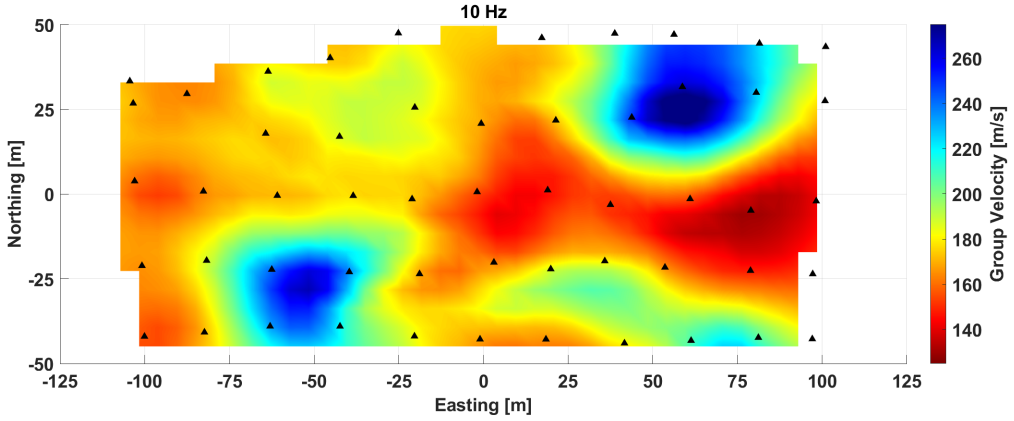

Figure A.21 10 Hz

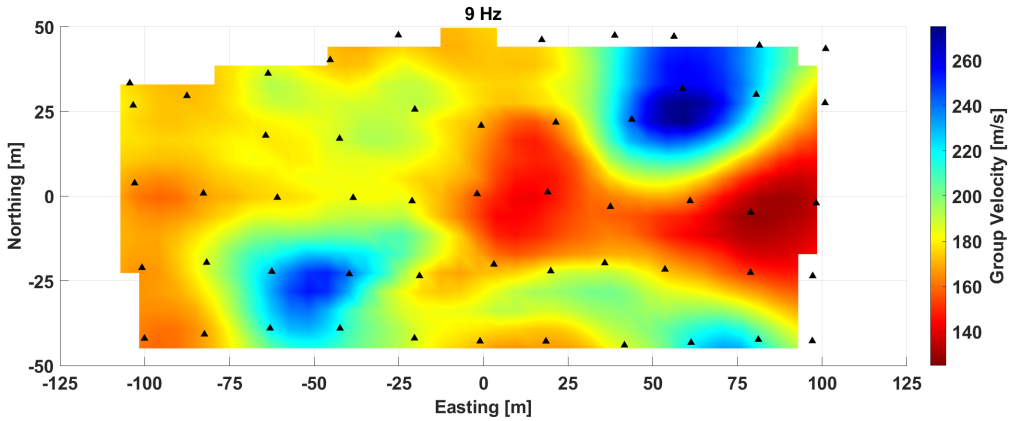

Figure A.22 9 Hz

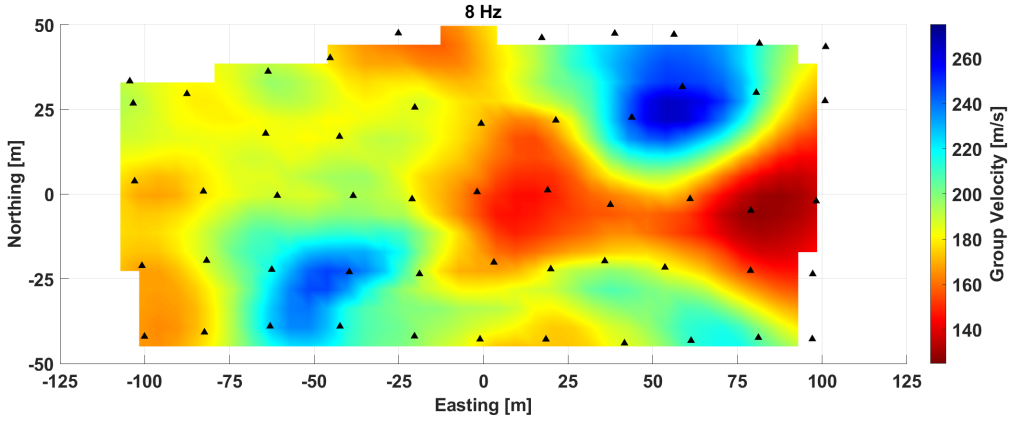

Figure A.23 8 Hz

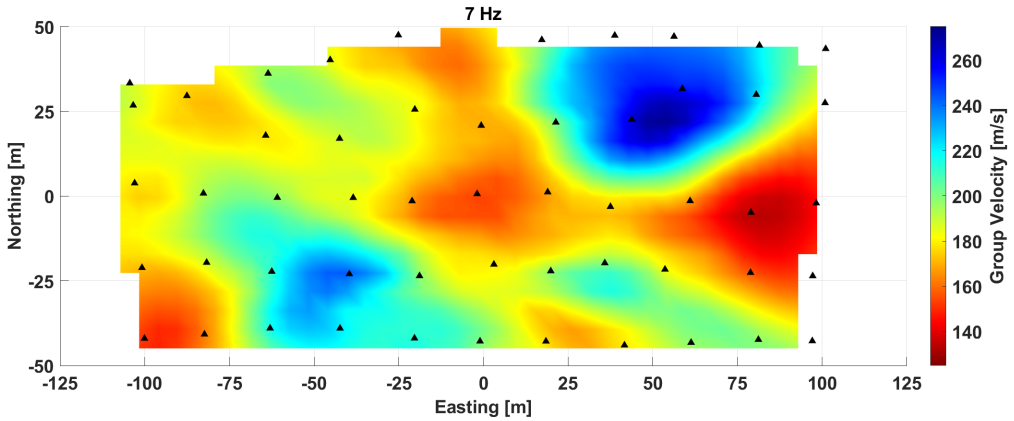

Figure A.24 7 Hz

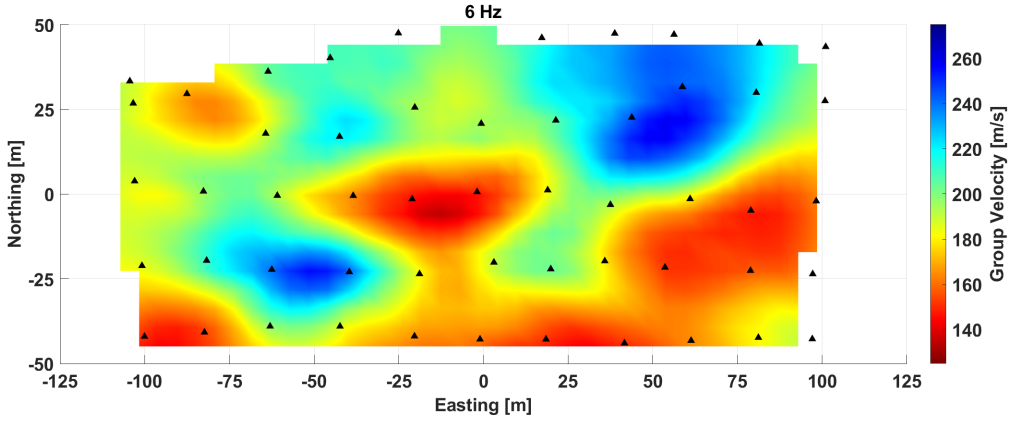

Figure A.25 6 Hz

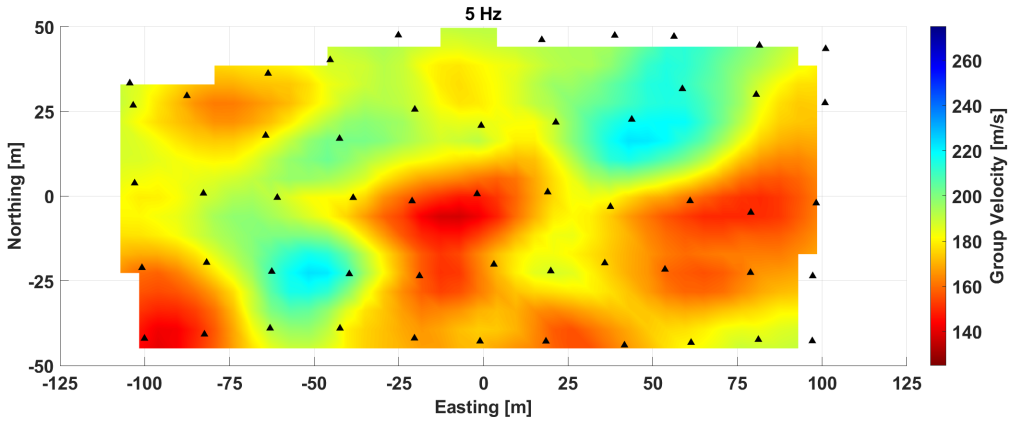

Figure A.26 5 Hz

APPENDIX B:

SELF POTENTIAL METHOD

B.1 Results

The self-potential model was spatially constrained by the bounds of the passive seismic array, with seismic station locations shown in Figure B.1 as black triangles superimposed on the self-potential map. The self-potential model showed distinct negative point anomalies as localized regions of dark blue.

A clear majority of these negative-valued self-potential anomalies were located in the western half of the survey area from -100 m E to 0 m E. An isolated negative-valued anomaly surrounded by higher self-potential was found at 25 m E 35 m N.

While the western half of the study area bounded by the passive seismic array exhibited more variation in self-potential, the eastern half was found to have mostly areas of positive self-potential with variation from 0 to 40 mV. Distinct positive-valued point anomalies roughly 15 m in diameter with values approaching 30 mV were visible throughout the eastern half of the study area. The southeastern corner of the study area showed consistently high self-potential values, as did the area near the far eastern edge of the site (90 m E to 100 m E). There is a significant point anomaly of high self-potential near 75 m E -25 m N. The variation in self-potential values over the entire study area was on the order of 100 mV. One strong dipole feature was present at -30 m E -30 m N with another possible dipole slightly to the north at -30 m E -5 m N.

B.2 Discussion

Point anomalies of negative self-potential shown in Figure B.1 are most likely zones of infiltration and preferential downward aquifer recharge which are related to subsurface karst expression, including covered sinkholes and associated conduits.

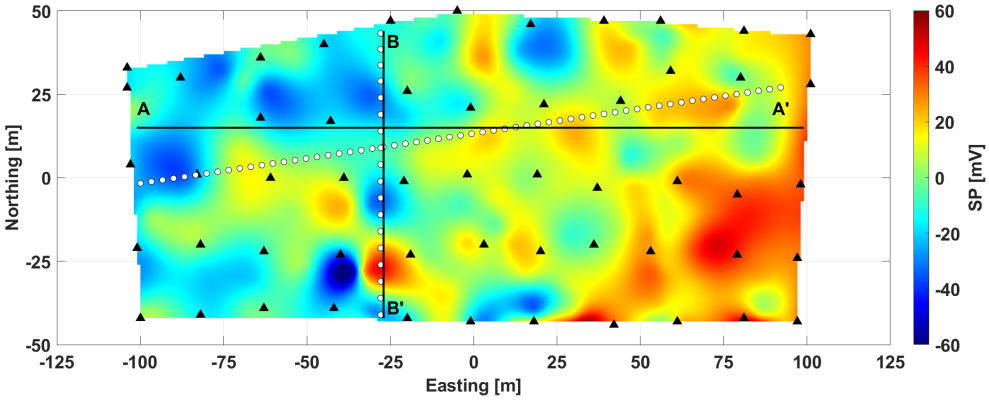

Figure B.1 Self-potential survey of GeoPark site with superimposed passive seismic station locations as black triangles, electrical resistivity lines as white circles and cross section reference locations A-A' and B-B'.

High self-potential areas near the southernmost edge of the survey between 25 m E and 100 m E and along the far eastern boundary are likely artifacts due to the electric lines and light poles both bordering the parking lot in the southern half of the study area and Magnolia Drive to the east (see Figures 2.1 and 2.2). The positive self-potential anomaly near 75 m E -25 m N could be evidence of localized upward fluid flow or an artifact of soil moisture drier than the surrounding area. It is difficult to constrain flow patterns in karst environments from a single survey, as groundwater can have erratic or tortuous flow paths and such paths can be seasonally-dependent.

Zones of moderately high self-potential near the center of the study area (25 m E 15 m N, 10-30 mV) could indicate shallow impermeable layers. The two possible electric dipole anomalies near -30 m E -25 m N could result from buried metal sprinkler pipes.

The self-potential results are inconclusive, though it is possible and certainly likely given the variability of karst structure that the surface expression of downward flow through a conduit would not appear precisely above a subsurface void. At the suspected sinkhole location of 25 m E 10 m N, the surface expression of self-potential is moderately positive surrounded by neutral or negative self-potential, which can be explained by the compaction of fine-grained sediments moving with gravity into a void.

The self-potential data does not add to the resistivity profiles as the SP method as applied here captures only a single moment in time within a dynamic hydrologic system. A 20-day record of self-potential measurements comparable to the seismic noise record would be informative for resolving typical locations of gravity-driven groundwater flow.